Geophys. J. Int. (1992) **111**, 363–390

Generalized seismological data functionals

Lind S. Gee* and Thomas H. Jordan

Department of Earth, Atmospheric and Planetary Sciences, Massachusetts Institute of Technology, Cambridge, MA 02139, USA

Accepted 1992 May 21. Received 1992 May 20; in original form 1991 October 31

SUMMARY

We have formulated a new waveform-analysis procedure to recover phase and amplitude information from individual seismograms that makes use of the ability to compute complete seismograms from realistic earth models. The basic tool is the isolation filter, a composite waveform constructed to select data from a desirable portion of the seismogram. When the cross-correlation between this synthetic waveform and an observed seismogram is localized in the time domain by windowing and in the frequency domain by narrow-band filtering, the resulting cross-correlagram can be approximated by a five-parameter Gaussian wavelet. One of these five parameters is the bandwidth of the correlagram, specified by the narrow-band filter; the other four define a set of time-like, frequency-dependent quantities $\{\delta t_x : x = \mathrm{q, p, a, g}\}$, which are functionals of earth structure. δt_p is the differential phase delay and δt_g is the differential group delay of the observed waveform relative to the synthetic, and δt_q and δt_a are the corresponding frequency-dependent amplitude parameters. We have developed a procedure for measuring the four generalized seismological data functionals by fitting a Gaussian wavelet to the windowed, filtered cross-correlagram. To relate the GSDFs to earth structure, we apply corrections to the differential times for the effects of windowing and filtering. Solving a linear system of four equations in four unknowns yields a set of differential dispersion parameters $\{\delta\tau_x : x = \mathrm{q, p, a, g}\}$. Formulae expressing the perturbations of the GSDFs in terms of the perturbations to the dispersion parameters for the individual component waveforms, including all interference effects, have been derived. Under a set of approximations valid for a large class of isolation filters, these can be simplified to yield easily computed expressions for the Fréchet kernels of the $\delta\tau_x$'s. The calculation of these Fréchet kernels requires no high-frequency approximations, and it can be extended to the investigation three-dimensional earth structure.

Key words: isolation filter, seismograms, structural inverse problem, waveform analysis.

1 INTRODUCTION

A major focus of seismological research concerns the development of techniques for extracting information from seismograms and using this information to construct earth models—the structural inverse problem. Methods established over the last decade or so have allowed seismologists to investigate the three-dimensional structural variations associated with mantle and core dynamics (e.g., Dziewonski & Woodhouse 1987; Jordan, Lerner-Lam & Creager 1989). Despite some notable achievements, there is still no consensus on a number of critical issues, including the dynamical implications of upper mantle anisotropy, the boundary layer structure of the core–mantle interface, and the long-standing controversy regarding chemical stratification in the mid-mantle transition zone. Although progress will certainly continue to be made by the application of existing methodologies to the growing catalogue of digitally recorded seismograms, it can be accelerated by improving the quality, as well as the quantity, of data available for the structural inverse problem.

The purpose of this paper is to introduce a waveform analysis procedure that can isolate new types of phase and amplitude information from individual seismograms. We motivate the analysis by discussing some general aspects of structural inverse problems, and we illustrate some of the

* Now at: Seismographic Station, UC Berkeley, Berkeley, CA 94720, USA.

Downloaded from https://academic.oup.com/gji/article/111/2/363/753853 by guest on 25 August 2022

advantages of the proposed methodology by applying it to a simple but interesting observational problem taken from a previous study of upper mantle anisotropy. We then derive the basic theory of generalized seismological data functionals, including the first-order perturbation theory needed to set up structural inverse problems. Later papers will discuss general methods for the construction of isolation filters and will apply the theory to various observational problems.

2 A PRACTICAL PHILOSOPHY FOR STRUCTURAL INVERSE PROBLEMS

We can represent a seismogram $s(t)$ as a sum over waveforms $\{u_n(t): n = 1, 2, \ldots\}$,

$$s(t) = \sum_{n=1}^{\infty} u_n(t), \tag{1}$$

where a particular element $u_n(t)$ may be a body-wave pulse, a travelling-mode wave train, or any other convenient representation. Each waveform $u_n(t)$ is described by a series of kinematical and dynamical properties—traveltime, amplitude, dispersion, etc.—which are functions of the seismic source, the recording instrument, and the path travelled by the particular wave group. The classical approach in structural seismology is to separate the process of estimating waveform properties from the process of inverting for model parameters (Fig. 1). Discrete body-wave pulses are identified and their traveltimes and amplitudes are measured; surface-wave groups are isolated and their dispersion and attenuation properties are determined. These data are then inverted for an earth model whose parametrization is sufficiently complete to explain the observed variations. If a good starting model is available, the latter step may be accomplished using a perturbation theory based on the variational principles of Fermat and Rayleigh.

One problem with this approach is interference by other arrivals. Indeed, portions of the seismogram where many wave groups arrive simultaneously cannot generally be resolved into either individual body waves or surface waves, and measurement schemes that rely on waveform isolation may not produce reliable results. Techniques based on frequency–wavenumber filtering have been used to separate

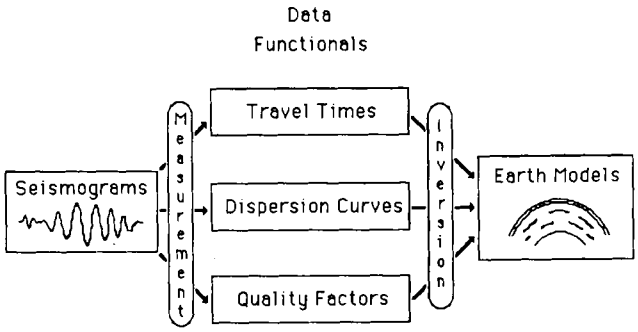

Figure 1. 'Classical' methodology separates the problem of determining earth structure into two parts: the measurement of well-defined data functionals, such as body-wave traveltimes and surface-wave dispersion, and the inversion of these data for earth models.

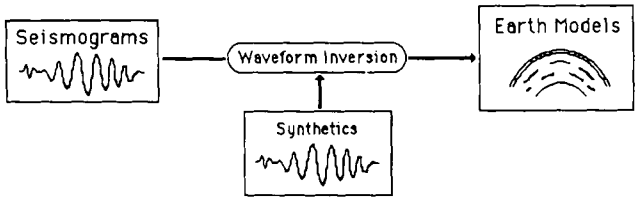

Figure 2. Waveform-inversion techniques build on current knowledge of earth structure through the construction of synthetic seismograms. The difference between the observed and synthetic seismograms is inverted directly for model perturbations.

interfering groups of body waves (e.g. Capon 1969; Julian, Davies & Sheppard 1972; Vinnik 1977) and surface waves (e.g. Nolet 1977; Cara 1979), but they generally require the heavy processing of signals from arrays of seismometers not common in global studies of earth structure. Moreover, their ability to resolve individual components is always finite, and the bias due to residual interference is sometimes difficult to assess.

Many of these difficulties can be avoided by inverting the complete seismogram directly for earth structure (Fig. 2). In the ideal situation when the entire wavefield is recorded by a spatially dense set of receivers from a spatially dense set of sources, non-linear image-reconstruction techniques can be applied to recover an image of the three-dimensional structure (Tarantola 1986). Although the collection of these sorts of ideal data sets can be approached in exploration seismology, where the effort and resources concentrated on imaging small volumes of the earth are high, the data sets available to global seismology are limited by the distribution of large-magnitude sources, primarily earthquakes, and the sparse distribution of stations, especially those with high-quality, digitally recording seismometers. In this situation, non-linear constructive methods cannot be applied because of the undersampling, and the manifold of models consistent with the data can have a very complex structure with many local minima. Global optimization methods such as simulated annealing (Rothman 1985) or genetic algorithms (Scales, Smith & Fischer 1991) are potentially useful for investigating this manifold, but the available codes are still primitive and can be immensely costly. In practice, therefore, the most feasible approach is based on the gradient method, which requires the problem to be linearized by assuming the solution is in some sense close to a chosen reference earth model.

Theoretical and computational advances over the last two decades now permit the routine calculation of synthetic seismograms $\bar{s}(t)$ using a variety of waveform representations. As in the case of equation (1), a seismogram computed from a reference earth model $\bar{\mathbf{m}}$ can be written as a sum over synthetic waveforms $\{\bar{u}_n(t)\}$,

$$\bar{s}(t) = \sum_{n=1}^{N} \bar{u}_n(t), \tag{2}$$

although N, the number of elements in the sum, is necessarily finite. Synthetic seismograms can accurately model wave propagation through realistic earth structures, as well as source and instrument effects. Most waveform inversion algorithms (Mellman 1980; Dziewonski & Steim 1982; Woodhouse & Dziewonski 1984; Tanimoto 1984,

Downloaded from https://academic.oup.com/gji/article/111/2/363/753853 by guest on 25 August 2022

1987) subtract synthetic seismograms from the observed time series to form differential seismograms that are then inverted for a structural perturbation using first-order perturbation theory. The linearized inverse problem thus takes the form

$$\mathbf{G}\,\delta\mathbf{m} = \delta\mathbf{s}, \tag{3}$$

where $\delta\mathbf{s}$ is a vector containing the differential time series, $\delta\mathbf{m}$ is the model perturbation, and $\mathbf{G}$ is a matrix of partial derivatives.

Among the drawbacks of waveform inversion are its generality and 'black box' character, which make it difficult to deal with the uneven distribution of structural information on real seismograms. Consider, for example, the differences between phase and amplitude observations. The phase data contained in traveltime measurements are robust, because the variational principles imply that their first-order variations depend only on the zeroth-order wavefields; in particular, rules can be constructed on how linear averages of phase data are, to first-order, related to linear averages of the model parameters (Jordan 1980). Similar averaging rules are generally not available for amplitude data, which can be very sensitive to minor features in the earth that are impractical to include in model parametrizations. The long-standing recognition of this distinction explains why seismologists who study earth structure have concentrated on the measurement of traveltimes or equivalent parameters, such as surface-wave phase velocities and normal-mode eigenfrequencies.

In simple waveform-inversion algorithms, however, amplitude information gets scrambled together with phase information, and it is usually not possible to assess the contributions of specific features on the seismograms to particular aspects of the resulting model, making it hard to evaluate the resolving power of the data set and to identify the robust features of the solution. Moreover, the results can be sensitive to how the data are weighted. Because the modelling assumptions are inadequate to describe many of the wave arrivals—most of the noise is 'signal-generated'—the statistical properties of the noise (e.g. its correlation structure) are not known, and any data weighting scheme is highly subjective. Finally, owing to the harmonic nature of band-limited signals and the possibility of cycle-skipping errors, the assessment of how well a synthetic matches an observed seismogram is ambiguous, making the inverse problem for differential seismograms highly non-linear. Waveform-inversion schemes tend to lock into spurious local minima if the starting model is not very close to the actual earth. Consequently, one of the purported advantages of waveform inversion, fully automated analysis, is largely illusory.

Seismologists now recognize that waveform inversion is no panacea and have begun to formulate more sophisticated approaches for extracting information from the seismogram. Recent examples include Cara & Lévêque's (1987) method to invert wave group envelopes, Nolet's (1990) partitioned waveform inversion, and Luo & Schuster's (1991a) inversion of 'skeletalized' data. One strategy, closely related to the approach adopted here, has been developed for travelling modes by Lerner-Lam & Jordan (1983). They have posed the linearized inverse problem in terms of the difference between the observed cross-correlation function, or cross-correlagram, $C_{ms}(t) \equiv \tilde{u}_m(t) \otimes s(t)$, and the model-predicted cross-correlagram, $\bar{C}_{ms}(t) \equiv \tilde{u}_m(t) \otimes \bar{s}(t)$, where $\tilde{u}_m(t)$ is the synthetic for the mth mode. This type of waveform inversion has the merit that a set of mode branches can be chosen to emphasize information on the seismogram of particular significance to the inverse problem at hand. Since the information about the differential dispersion of the mth mode is concentrated near the peak of its cross-correlagram, where the signal-to-noise ratio (SNR) is typically the highest, windowing is effective in isolating this information from other signals. Because a number cross-correlagrams can be constructed from a given seismogram, it is easy to implement differential weighting schemes (e.g. downweighting the high-amplitude surface waves) to improve the resolution and variance of the model parameters (Lerner-Lam & Jordan 1983, 1987; Gee, Lerner-Lam & Jordan 1985).

The waveform-analysis procedure formulated in this paper departs from the method of Lerner-Lam & Jordan (1983) by employing the cross-correlation of synthetics with observed seismograms to measure and interpret frequency-dependent traveltimes and related data functionals (Fig. 3), rather than inverting differential cross-correlagrams directly for earth structure. It is closely related to the 'wave-equation traveltime inversion' recently discussed by Luo & Schuster (1991a,b), which also formulates traveltime functionals in terms of cross-correlagrams. Whereas Luo and Schuster's technique considers a single traveltime defined by the correlagram peak, ours extracts a more complete set of information from each correlagram. To define the correlagram, we employ a type of synthetic seismogram we call an isolation filter.

An isolation filter, $\bar{f}(t)$, is a weighted sum of wave groups synthesized from a reference earth model:

$$\bar{f}(t) = \sum_{n=1}^{N} \alpha_n(t) * \tilde{u}_n(t). \tag{4}$$

The asterisk denotes convolution of the nth synthetic wave group $\tilde{u}_n$ with an arbitrary filter α_n. Examples of isolation

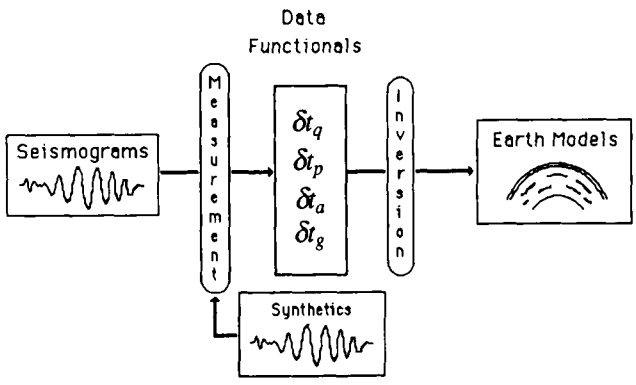

Figure 3. The methodology discussed in this paper combines the advantages of the classical approach with those of waveform inversion. Synthetic seismograms constructed from a reference earth model are used to extract 'generalized data functionals' from a selected wave group at a particular frequency, and these data are subsequently inverted for a improved earth model. The measurement process and the formulation of Fréchet kernels account for wave effects such as caustic phase shifts, dispersion, diffraction, and interference by other wave groups.

Downloaded from https://academic.oup.com/gji/article/111/2/363/753853 by guest on 25 August 2022

filters include individual body-wave arrivals such as *S*-waves, dispersed wave trains such as the fundamental-mode Love and Rayleigh waves, and general sums over travelling modes constructed to represent complex wave groups, such as *Sa*. In fact, isolation filters need not correspond to any particular waveform in the standard taxonomy of seismic phases; for example, the α_n may be chosen so that $\tilde{f}$ samples a particular region—e.g. the mid-mantle transition zone, *D''*, or even the inner core—in some specified way.

To process an observed seismogram using a particular isolation filter, we apply two basic operations to the cross-correlagram $C_{fs}(t) \equiv \bar{f}(t) \otimes s(t)$. The first localizes the signal in the time domain by zeroing $C_{fs}(t)$ outside of a finite window centred at the peak of the cross-correlagram. The second localizes the signal in the frequency domain by narrow-band filtering the windowed cross-correlagram about a set of reference frequencies $\{\omega_i\}$. The parameters controlling the time-domain and frequency-domain localizations can always be chosen such that the output of these operations is well approximated by a Gaussian wavelet; i.e. as a monochromatic carrier modulated by a Gaussian envelope. We show that, when this approximation is enforced, the wavelet depends upon only four functionals of earth structure, two amplitude and two phase parameters. These four observables define the generalized seismological data functionals. The theory allows us to characterize these observables as well-defined functionals of earth structure; in particular, it yields Fréchet kernels that can be employed in linearized inversion for earth models. For simplicity, we shall present explicit expressions of these functional derivatives for only a one-dimensional, radially stratified model. Their generalization to two and three dimensions via the Born approximation (Woodhouse 1983; Tromp & Dahlen 1990) is straightforward.

The inversion of the generalized data for earth structure is thus separated from their measurement, as in the classical methodology of Fig. 1, permitting 'hands-on' assessments of the data quality and model robustness. Furthermore, the measurement procedure in the first step of Fig. 3 is much less susceptible to the cycle-skipping errors that often plague waveform inversion, and the inverse problem in the second step requires only the linearization of the relationship between the model and functional differentials, not between the model and differential seismograms.

3 AN EXAMPLE APPLICATION: OBSERVATIONS OF *Sa* FOR A EURASIAN PATH

While the concepts underlying the theory are simple, its mathematical details are rather complex. We fix some of the ideas and notation by illustrating, cookbook style, the application of the analysis procedures to an observational example. The seismograms are from a deep-focus Sea of Okhotsk earthquake (01 Feb 84, $h = 581$ km) recorded at the Global Digital Seismic Network (GDSN) station GRFO ($\Delta = 74.3°$). Fig. 4 plots the data $s(t)$ for the long-period vertical (LPZ) and transverse (LPT) components between 18 and 34 min after the origin time and compares them with the synthetics $\bar{s}(t)$ computed for the EU2 model of Lerner-Lam & Jordan (1987). All time series have been low-pass filtered with an upper cut-off at 50 mHz. The

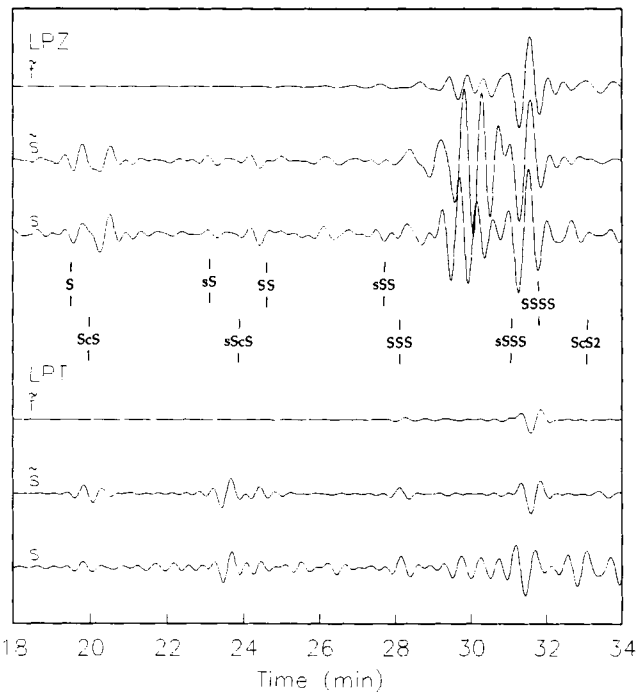

Figure 4. $\tilde{f}(t)$, $\bar{s}(t)$, and $s(t)$ for an earthquake source in the Sea of Okhotsk (02/01/84, $h = 581$ km) recorded at the Global Digital Seismic Network station GRFO ($\Delta = 74.3°$). The rotated and filtered seismograms for the vertical (LPZ) and transverse (LPT) components are plotted with the isolation filters and the complete synthetic seismograms calculated by normal-mode summation from model EU2 (Lerner-Lam & Jordan 1987) appended to a PREM lower mantle (Dziewonski & Anderson 1981). The waveforms represented by $\tilde{f}(t)$ comprise multiply reflected *S* phases and their near-surface interactions and are referred to as '*Sa*' on both components.

agreement between the data and synthetics is good for the various body waves having turning points in the lower mantle, i.e. from direct *S* up to and including *SSS*, but is less favourable for the large *Sa* wave groups coming in after 29 min, which contain energy propagating primarily through the upper mantle. At this distance, *Sa* can be represented as a superposition of multiply reflected body waves, including triplicated *SSSS* and, on the vertical component, various *P–SV* interconversions, or as a superposition of higher modes, primarily the first through sixth Love and Rayleigh overtones (Caloi 1953; Båth & Lopez-Arroyo 1963; Brune 1964; Schwab, Kausel & Knopoff 1974; Cara 1976).

A close examination of Fig. 4 reveals an apparent inconsistency in the traveltimes of *Sa*: the observed waveform arrives earlier with respect to the synthetic on the transverse-component than on the vertical-component. We have used this and other observations as evidence for strong shearwave splitting due to radial anisotropy in the uppermost mantle beneath Eurasia (Gee & Jordan 1988). Given the complexities in the wave interactions that produce these seismograms, however, it is possible that this apparent splitting is due to the different ways that the *SH* and *P–SV* waveforms sample an isotropic upper mantle structure. If EU2 does not properly represent this structure, then differences of the sort illustrated in Fig. 4 might occur

Downloaded from https://academic.oup.com/gji/article/111/2/363/753853 by guest on 25 August 2022

without any anisotropy. The theory presented in this paper allows a uniform methodology to be applied to multicomponent data sets and is particularly well suited to resolving this kind of analysis problem. We shall carry out a step-by-step application of our techniques to the *Sa* data in Fig. 4, beginning with the construction of isolation filters and proceeding through the measurement and interpretation of the frequency-dependent traveltimes.

3.1 Construction of the isolation filters

The isolation filters for this problem are synthetic seismograms of the *Sa* phase on the transverse and vertical components. The seismograms are represented as sums over travelling modes, so that $\tilde{u}_n(t)$ in equation (4) is the synthetic for the $(n-1)$th Love or Rayleigh overtone (i.e. $n=1$ is the fundamental mode). These mode-branch seismograms are computed using the Harvard centroid–moment tensor (CMT) mechanism (Dziewonski, Franzen & Woodhouse 1984). The synthesis is done in the frequency domain by setting the weights $\alpha_n(\omega)$ proportional to a Gaussian function whose argument varies as the difference of the group delay computed for $\tilde{u}_n(\omega)$ with respect to some reference arrival time t_{Sa}. We adopt the value $t_{Sa}=31.5$ min, which corresponds to a group velocity of $4.36\,\mathrm{km\,s^{-1}}$, and select the half-width of the Gaussian to restrict contributions to an effective group-velocity window of 4.2–$4.5\,\mathrm{km\,s^{-1}}$. In performing this calculation, we must add the group delays of the source and instrument to the group traveltime. The inverse Fourier transform then yields time series corresponding to a stationary, phase-like approximation to *Sa*. As seen in Fig. 4, the transverse-component isolation filter computed by this algorithm comprises a single pulse similar to the *Sa* arrival on the complete synthetic, while the vertical-component isolation filter contains some additional energy associated with shear-coupled *PL* modes propagating in the crustal waveguide, which arrive prior to *Sa*. Although it is possible to formulate a *P–SV* isolation filter that selectively eliminates the *PL* modes, and thus provides a sampling of upper mantle structure more equivalent to the *SH* isolation filter, we have not attempted to do so for this exercise, since one of our goals is to illustrate how the theory accounts for the complexities of *P–SV* mode coupling.

3.2 Computation of the cross-correlagrams

Because the earth model is an inaccurate description of the structure along this particular path, the *Sa* synthetics do not match the data. The information about these differences can be concentrated by forming the cross-correlation of the isolation filter with the observed seismogram, $C_{fs}(t)\equiv\tilde{f}(t)\otimes s(t)$, shown in Fig. 5(a). The amplitude spectrum of $C_{fs}(t)$, denoted $|C_{fs}(\omega)|$, where ω is angular frequency, is bandlimited by the GDSN instrument response and the low-pass filter applied to the seismograms. If the synthetic properly models these filters, then this amplitude spectrum will approximate the autocorrelation spectrum $\tilde{C}_{ff}(\omega)=\tilde{f}^*(\omega)\tilde{f}(\omega)$, which we parametrize by a frequency centroid $\tilde{\omega}_c$ and half-bandwidth $\tilde{\sigma}_c$. For the *SH* isolation filters in Fig. 4, a Gaussian approximation to $\tilde{C}_{ff}(\omega)$ yields $\tilde{\omega}_c/2\pi=28.4$ millihertz (mHz) and $\tilde{\sigma}_c/2\pi=8.1$ mHz. [NB. Throughout this paper, tildes will be placed over functions derived by cross-correlating the isolation filter with any synthetic seismogram, including $\tilde{f}(t)$ itself, and over the spectral parameters derived from them.]

$\tilde{C}_{ff}(t)$ is, by definition, an even function, whereas $C_{fs}(t)$ is asymmetric and displaced from zero lag by the phase

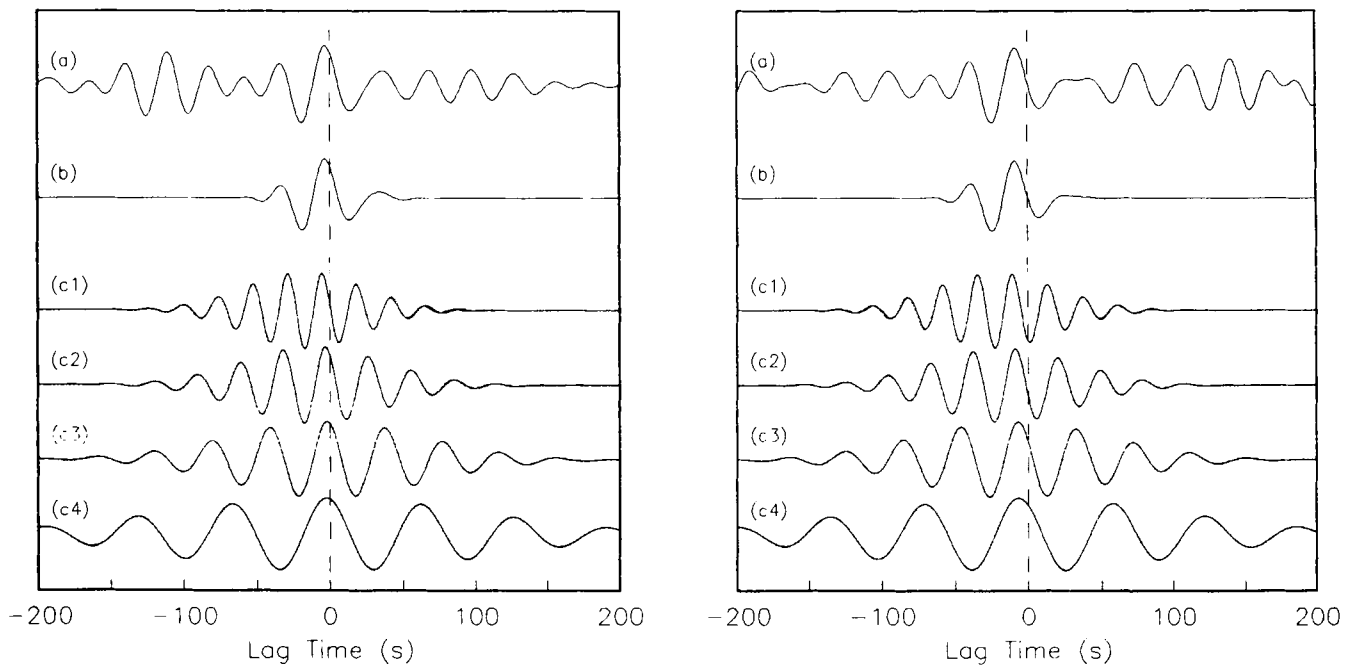

Figure 5. Illustration of the analysis procedures for the vertical (left) and transverse (right) components of the *Sa* example. (a) The cross-correlation function $C_{fs}(t)$. (b) The windowed correlation $WC_{fs}(t)$. (c) The filtered and windowed correlation $F_iWC_{fs}(t)$ for four filters with the analytic correlation functions obtained from minimizing equation (7) (dotted lines).

Downloaded from https://academic.oup.com/gji/article/111/2/363/753853 by guest on 25 August 2022

difference between the data and the synthetic. The direct measurement of this phase difference is the basis for a class of digital processing techniques commonly applied in the study of fundamental-mode dispersion, most notably the residual dispersion method of Dziewonski, Mills & Bloch (1972) and the phase-matched filtering method of Herrin & Goforth (1977). In our example, the peak of $C_{fs}(t)$ occurs at a lag-time that is about 6 s more negative on the transverse component than on the vertical component, consistent with the traveltime differences observed directly on the time series. It can be shown that the peak shift is an estimate of the differential phase delay between the data and synthetic at the centre frequency $\bar{\omega}_c$, provided $\xi_0^2 = (\bar{\sigma}_c/\bar{\omega}_c)^2 \ll 1$ (Jordan 1980). For the data in Fig. 5(a), this squared ratio equals 0.08, so that the approximation is justified.

3.3 Time-domain localization by windowing

Near zero lag the cross-correlagrams are dominated by the *Sa* phase, but at larger lag-times they exhibit complexities associated with other wave groups. To reduce the influence of these interfering arrivals on our measurements, we localize the signal in the time domain by multiplying $C_{fs}(t)$ by a windowing function $W(t)$ that is non-zero only over some interval of total length T_w. The windowed cross-correlagrams, $WC_{fs}(t) \equiv W(t)C_{fs}(t)$, displayed in Fig. 5(b), were computed using 140 s Hanning tapers centred at the peak of $C_{fs}(t)$. A squared-cosine window of this length has a Fourier transform with a corner frequency $\sigma_w/2\pi \approx 0.72/T_w = 5.2$ mHz. By localizing the signal in the time domain, it acts to increase the effective half-bandwidth from $\bar{\sigma}_c/2\pi = 8.1$ mHz to approximately $(\sigma_w^2 + \bar{\sigma}_c^2)^{1/2}/2\pi = 9.6$ mHz.

In most applications of the residual dispersion technique to surface waves, the phase spectrum of a cross-correlagram is interpreted in terms of the dispersion of a single (e.g. fundamental) mode, which requires that the interference from modes not included in the phase-matched filter be small. Windowing in the time domain is commonly employed to suppress the distortion of the phase spectrum by extraneous signals (Herrin & Goforth 1977). The theory presented here also uses windowing to achieve time-domain localization, but this tapering operation need not completely eliminate the interference of arrivals excluded from $\bar{f}$, since we shall account for such interference effects in the interpretation of the data. This aspect of the theory is a major advantage of our technique over standard residual-dispersion methods.

3.4 Frequency-domain localization by narrow-band filtering

The next step in our analysis scheme is to localize the signal in the frequency domain by convolving the windowed cross-correlagram with a set of narrow-band filters, $\{F_i WC_{fs}(t) \equiv F_i(t) * [W(t)C_{fs}(t)] : i = 1, 2, \ldots, I\}$. We typically use zero-phase filters with approximately Gaussian spectra of the form $F_i(\omega) \sim \exp[-(|\omega| - \omega_i)^2/2\sigma_i^2]$, where the ratio of the half-bandwidths σ_i to the centre frequencies ω_i are chosen to be much less than unity. The solid lines in Fig. 5(c) show the *Sa* results for $\sigma_i/\omega_i = 0.1$ at four centre frequencies: $\omega_i/2\pi = 45$, 35, 25, and 15 mHz.

The key to our theoretical treatment is the realization that each of the narrow-band waveforms produced by this sequence of operations is well approximated by a function $g(t)$ which is the product of Gaussian envelope and a harmonic carrier:

$$F_i WC_{fs}(t) \approx g(t) \equiv A\,\mathrm{Ga}[\sigma_s(t - t_g)]\cos[\omega_s(t - t_p)]. \tag{5}$$

Here $\mathrm{Ga}(x)$ denotes the unnormalized Gaussian function $e^{-x^2/2}$. As discussed in Appendix A, such waveforms are called five-parameter Gaussian wavelets. In the vicinity of the carrier frequency $\omega_s > 0$, the Fourier spectrum of the Gaussian wavelet is

$$g(\omega) \approx \frac{A\sqrt{2\pi}}{\sigma_s}\,\mathrm{Ga}\left[\frac{\omega - \omega_s}{\sigma_s}\right]\exp[i(\omega_s t_p + (\omega - \omega_s)t_g)], \tag{6}$$

where the approximation ignores the spectral peak centred at $-\omega_s$. A Gaussian wavelet's amplitude spectrum $|g(\omega)|$ is thus characterized by three parameters, a positive scale factor A, a centre frequency ω_s, and a half-bandwidth σ_s; and its phase spectrum $\phi(\omega)$ is characterized by two parameters, a phase delay $t_p = \phi_s/\omega_s$ and a group delay $t_g = (d\phi/d\omega)_s$.

3.5 Definition and estimation of generalized data

The five parameters in the Gaussian-wavelet model are estimated by fitting the time-domain expression (5) to the filtered, windowed cross-correlagram using a weighted least-squares method. We seek a wavelet $g(t)$ that best approximates the correlagram $F_i WC_{fs}(t)$ in the vicinity of its peak, which occurs at some lag-time t_i. This is achieved by minimizing the quantity

$$\chi^2 = \frac{\int_{-\infty}^{\infty} [F_i WC_{fs}(t) - g(t)]^2 e^{-\gamma^2(t-t_i)^2}\,dt}{\int_{-\infty}^{\infty} g^2(t) e^{-\gamma^2(t-t_i)^2}\,dt}, \tag{7}$$

where γ is an angular frequency which scales a Gaussian weighting function centred at t_i. It can be shown that this procedure is equivalent to matching the low-order moments of the real-valued spectrum $F_i WC_{fs}(\omega)$ to those of the Gaussian spectrum given by (6). In applying this waveform-fitting procedure to the *Sa* example, we have chosen $\gamma \approx \sigma_i$, so that any variations in $F_i WC_{fs}(t)$ at lag-times larger than the envelope half-width of $g(t)$ are downweighted substantially in the error measure. Fig. 5(c) superimposes the five-parameter model obtained from the minimization (dotted lines) on the observed cross-correlagrams (solid lines). The agreement is excellent where the amplitudes are large, with only small differences evident on the flanks of the cross-correlagrams. In this example (as in most cases), a well-defined global minimum is obtained.

The interpretation of the wavelet parameters is particularly straightforward when three conditions are satisfied: (1) other arrivals do not interfere with the waveform $\bar{f}(t)$; (2) the spectrum of F_i is much narrower than that of WC_{fs}; and (3) ω_i is not too far removed from $\bar{\omega}_c$. Then, $\omega_s \approx \omega_i$ and $\sigma_s \approx \sigma_i$, and it follows that t_p and t_g will equal the differential dispersion of the data relative to the synthetic at ω_i, and A will measure their amplitude ratio. The requisite conditions are rarely achieved in practice,

Downloaded from https://academic.oup.com/gji/article/111/2/363/753853 by guest on 25 August 2022

however, and a more refined analysis is needed for a proper structural interpretation. Our procedure is to minimize a quadratic form like (7) to obtain a Gaussian-wavelet approximation to the filtered, windowed cross-correlagram between $\bar{f}(t)$ and the complete synthetic $\bar{s}(t)$:

$$F_i W \bar{C}_{fs}(t) \approx \bar{g}(t) \equiv \tilde{A}\, \mathrm{Ga}\,[\bar{\sigma}_s(t-\tilde{t}_g)] \cos\,[\bar{\omega}_s(t-\tilde{t}_p)]. \tag{8}$$

The apparent phase delay $\tilde{t}_p$ and group delay $\tilde{t}_g$ measure the interference between the isolation filter and other waveforms on the synthetic, and will be small when $F_i W \bar{C}_{fs}$ is approximated by the filtered, windowed autocorrelation function $F_i W \bar{C}_{ff}$. In the *Sa* example, the interference due to wavegroups excluded from $\bar{f}$ is negligible on the transverse component, but not on the vertical: at 25 mHz, for example, $\tilde{t}_p = -0.6$ s and $\tilde{t}_g = -4.2$ s. It is typical that the interference affects the group delay more than the phase delay.

To a very good approximation, the spectral widths of the cross-correlagrams are dominated by the various filters applied to the seismogram, which are known, and only weakly dependent on the unknown details of the propagation. Hence, the synthetics can be constructed such that $\sigma_s \approx \bar{\sigma}_s$. The differences between (5) and (8) can then be parametrized in terms of four time-like quantities. Two are the differential phase and group delays.

$$\delta t_p = t_p - \tilde{t}_p, \tag{9}$$

$$\delta t_g = t_g - \tilde{t}_g. \tag{10}$$

The third measures the difference in logarithmic amplitudes,

$$\delta t_q = -\frac{1}{\bar{\omega}_s}[\ln A - \ln \tilde{A}], \tag{11}$$

and the fourth measures the difference in centre frequencies,

$$\delta t_a = -\frac{1}{\bar{\sigma}_s^2}[\omega_s - \bar{\omega}_s]. \tag{12}$$

The quantities in (9)–(12) contain the information about earth structure extractable from $F_i W C_{fs}(t)$. Most data commonly derived from seismograms can be associated with, or related to, these four types of observables. Because the procedures we have described do not depend on the particular waveform of interest, we shall call them *generalized seismological data*. In setting up structural inverse problems, one considers a particular datum to be an estimate of a certain function of earth structure, called a gross earth data functional by Backus & Gilbert (1967). We shall use the term *generalized seismological data functionals*, abbreviated GSDF, to describe the functional relationships between the set of differential times $\{\delta t_x = t_x - \tilde{t}_x : x = \mathrm{q, p, a, g}\}$ and an earth model perturbation $\delta\mathbf{m} = \mathbf{m} - \bar{\mathbf{m}}$. One of the main purposes of this paper is to derive these functional equations.

Fig. 6 shows the values of the differential times estimated by applying the waveform-fitting procedure to the *Sa* cross-correlagrams using filters spaced at 5 mHz intervals across the band 10–45 mHz. An assessment of the uncertainties in these measurements will be deferred to a more comprehensive observational study. We note, however, that δt_q and δt_p are better determined parameters than δt_a and δt_g because they are fixed by variations which take place on the time-scale of the correlagram's carrier wave rather than its envelope. In this particular example, the standard errors associated with the former two are on the order of ± 1 s and those for the latter two are perhaps a factor of two larger, except near the low-frequency end of the band, where all of the measurement errors increase. The nearly constant offset between the δt_q data for the two components could plausibly be explained by a poor source model, but variations of the other measurements with frequency and component-type are indicative of significant variations between the path-averaged structure and the EU2 reference model.

In this initial paper, we discuss the functional equations for all four data types, but our attention is focused primarily on the differential phase delay δt_p, which has practical advantages in structural inverse problems. Observationally, it is more stable than the group delay with respect signal-generated noise. Theoretically, it is more easily interpreted than either the group delay or the two functionals describing the amplitude variations. As we shall discuss later in this paper, there is an approximation, often valid in practice, which allows us to take advantage of a variational principle when modelling the differential phase delay for an isolated waveform. The variational principle limits the sensitivity of this datum to wavefield distortions in the real earth not properly represented by the synthetics, thus simplifying the first-order relationship between δt_p and a perturbation to earth structure. It therefore becomes a relatively straightforward task to compute its Fréchet kernel.

The phase-delay residuals δt_p shown in Fig. 6 are negative for both the vertical and transverse components, implying that the average upper mantle velocities along this particular path are greater than EU2; moreover, they both show a similar frequency variation, characterized by concave-downward curvature. Most significant, the *SH* data are systematically offset by 5–6 s with respect to the *P–SV* data, matching the shift in the correlagram peaks noted earlier.

3.6 Fréchet kernels

To see if the δt_p offset in Fig. 6 requires anisotropy, we need to be able to assess how differently the *SH* and *P–SV* waveforms sample the velocity structure. This can be done by examining the Fréchet kernels that relate a path-averaged perturbation $\delta m(r)$ to perturbations in the phase-delay times. At a centre frequency $\bar{\omega}_s$, the perturbation will induce a change in the phase delay of the nth mode branch, which we denote by $\delta\tau_p^n(\bar{\omega}_s)$. The Fréchet kernel $g_p^n(\bar{\omega}_s, r)$ that maps the spherically symmetric perturbation $\delta m(r)$ into $\delta\tau_p^n(\bar{\omega}_s)$ is easily derivable from the eigenfrequency kernels for standing modes (Woodhouse & Dahlen 1978). We shall show that, to a good approximation, the phase-delay residuals δt_p can be corrected for windowing and filtering effects to obtain a differential time $\delta\tau_p$ whose Fréchet kernel can be written as a linear combination of the g_p^n's:

$$\delta\tau_p(\bar{\omega}_s) \approx \sum_{n=1}^{N} c_n \int_0^R g_p^n(\bar{\omega}_s, r)\, \delta m(r) r^2\, dr. \tag{13}$$

Downloaded from https://academic.oup.com/gji/article/111/2/363/753853 by guest on 25 August 2022

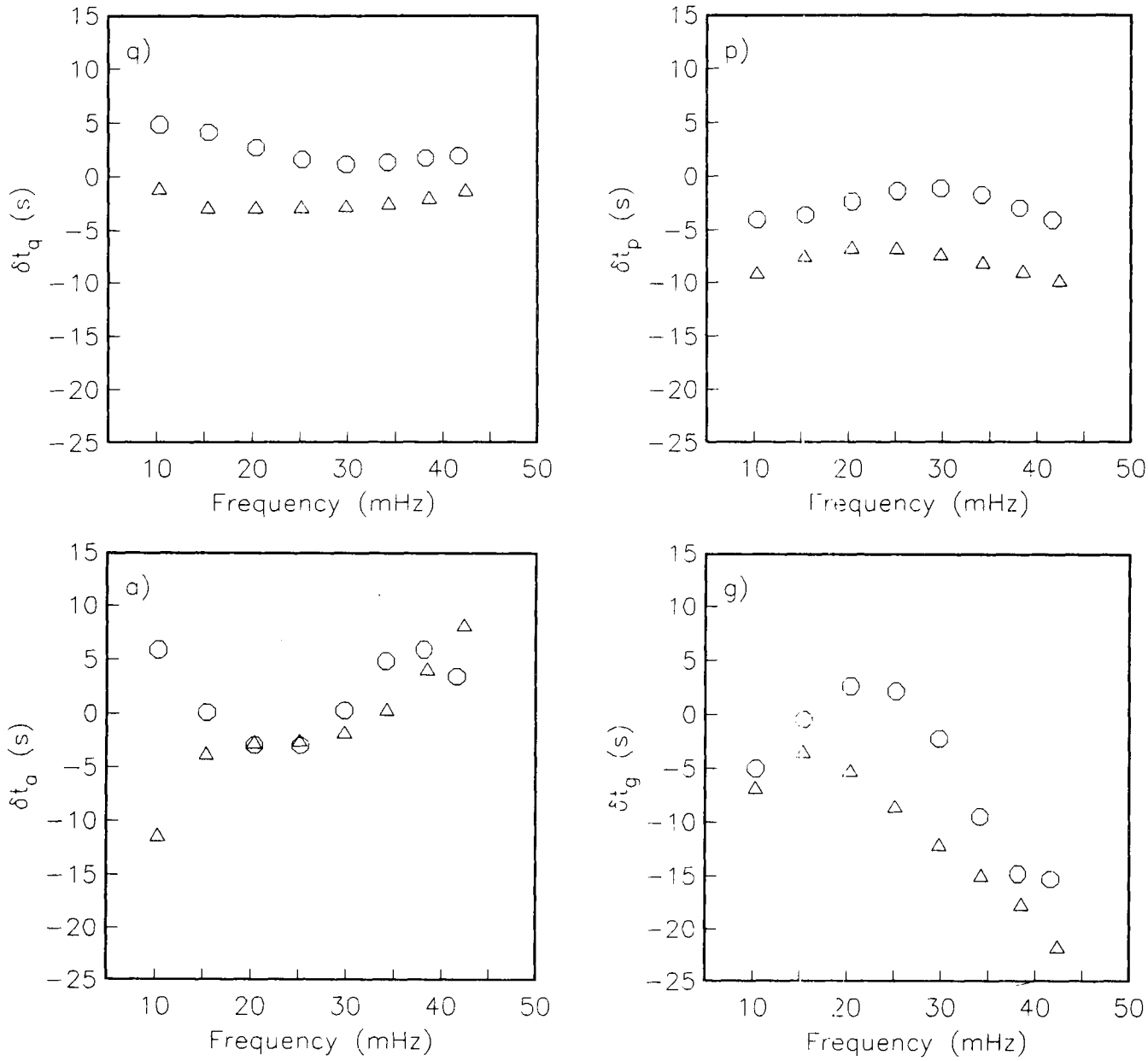

Figure 6. Generalized data functionals $\delta t_x (x = \mathrm{q}, \mathrm{p}, \mathrm{a}, \mathrm{g})$ obtained by applying the waveform fitting procedure to the *Sa* cross-correlagrams. The vertical (circles) and transverse (triangles) component measurements were made with filters applied at 5 mHz intervals in the band from 10–45 mHz.

The expressions for the coefficients c_n are themselves a sum over the travelling modes in the isolation filter, and they involve the source excitation and receiver response, as well as the various windowing and filtering parameters. Fig. 7 illustrates the kernels for the *Sa* example at the frequencies from 10 to 45 mHz for the case of an isotropic earth model. We see that the phase delay is primarily sensitive the shear velocity structure of the upper mantle and transition zone; for both polarizations, the density kernels oscillate about zero, and the compressional velocity kernels on the vertical component are very small. At low frequencies, the *P–SV* kernels oscillate more than the *SH* kernels, but averaged over an oscillation, their values are very similar. Above 25 mHz the *P–SV* kernels have shallower turning points—the exponential tails on the transverse component extend farther into the lower mantle—and above 35 mHz they exhibit a strong peak centred near the base of the crust. The latter is due to the existence of the *PL* energy in the *Sa* isolation filter, clearly evident in Fig. 4, which is governed by the shear velocity contrast across the Mohorovičić discontinuity. As a final feature of interest, we note that the *SH* kernels above 35 mHz display a low-amplitude oscillation in the lower mantle below their evanescent tails. This oscillatory behaviour, absent in the *P–SV* kernels, is caused by the interference of ScS_2, which arrives approximately two minutes after *Sa*.

A rigorous test of the anisotropy hypothesis would use the Fréchet kernels in Fig. 7 to search for an isotropic model that satisfies the phase-delay data in Fig. 6. If a reasonable model can be found, e.g. one which fits these data as well

Downloaded from https://academic.oup.com/gji/article/111/2/363/753853 by guest on 25 August 2022

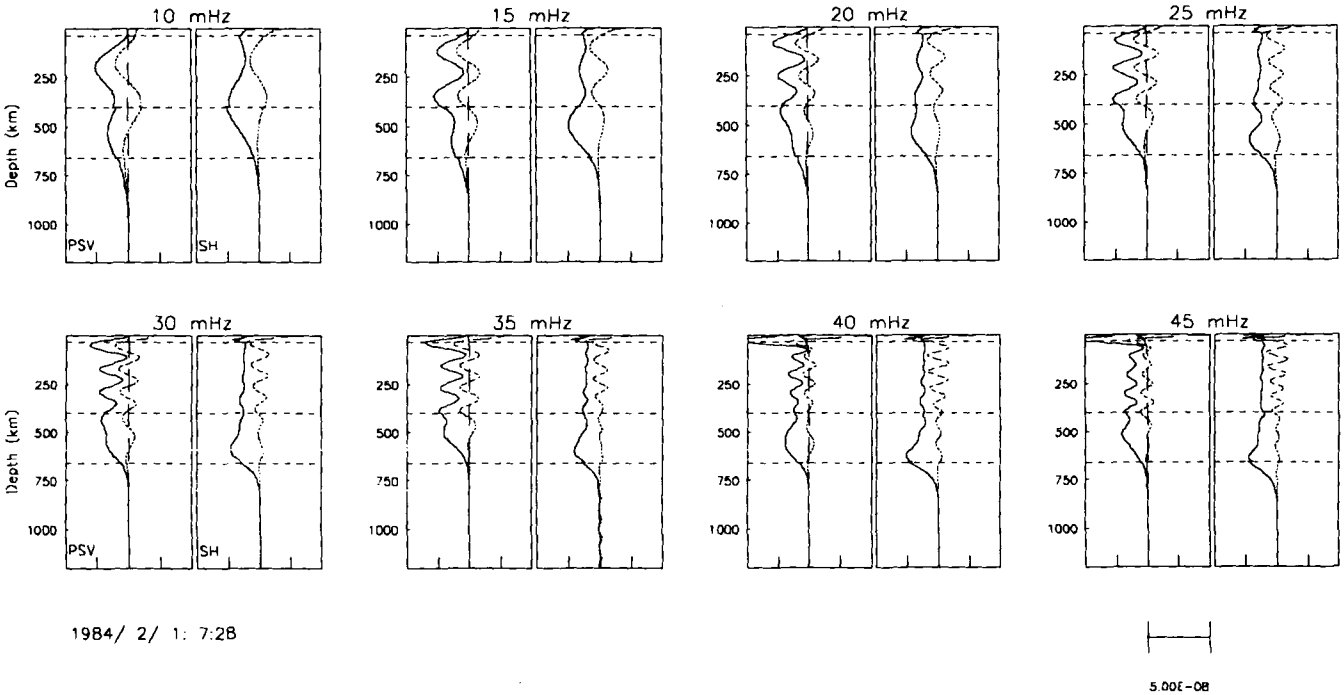

Figure 7. Vertical (*P–SV*) and transverse (*SH*) component Fréchet kernels for $\delta\tau_p$ in the band from 10–45 mHz, corresponding to the measurements illustrated in Fig. 6. The solid line is the shear velocity kernel, the short dashed line is the density kernel, and the long dashed line is the compressional velocity kernel. The location of the Mohorovičić and transition zone discontinuities are marked by horizontal lines. One tic interval on the horizontal axis represents 5×10^{-8} s km^{-3} unit^{-1} perturbation.

as, say, the phase-delay observations extractable from the surface waves and other phases on the seismograms of Fig. 4, then we might be able to conclude that anisotropy is unnecessary. A formal treatment of this inverse problem will not be attempted here, but it is clear that, given the similarity of the *SH* and *P–SV* kernels in Fig. 7, it will be extremely difficult to match the large traveltime differences observed for *Sa* with a smooth isotropic model. [It is always possible, of course, to mimic radial anisotropy with rough isotropic layering (e.g. Backus 1962; Gee & Jordan 1988)]. We surmise that, averaged over vertical scale lengths of a hundred kilometres or so, some type of radial anisotropy is required. Inversion to obtain such a path-averaged model can be accomplished by using the appropriate anisotropic kernels (Woodhouse & Dahlen 1978; Dziewonski & Anderson 1981) to compute the g_p^n's (Gaherty, Jordan & Gee 1992).

4 THEORETICAL DEVELOPMENT

Having outlined the methodology and introduced some of the notation in the previous section, we now proceed to fill in the theoretical details. The basic approximation underlying the theory is contained in equation (5): the representation of the filtered, windowed cross-correlagram by a Gaussian wavelet. The Gaussian-wavelet approximation emerges most naturally as the leading term of an expansion known as a Gram–Charlier series.

4.1 Autocorrelagram of the isolation filter

We first consider the autocorrelation function of the isolation filter $\bar{f}(t)$, defined by

$$\bar{C}_{ff}(t) \equiv \bar{f}(t) \otimes \bar{f}(t) = \int_{-\infty}^{\infty} \bar{f}(\tau)\bar{f}(\tau + t)\, d\tau$$

$$= \frac{1}{2\pi} \int_{-\infty}^{\infty} \tilde{C}_{ff}(\omega) e^{-i\omega t}\, d\omega. \qquad (14)$$

Since $\bar{C}_{ff}(t)$ is a real-valued, symmetric function peaked at zero lag, its Fourier spectrum $\tilde{C}_{ff}(\omega)$ is also real-valued and symmetric. We expand $\tilde{C}_{ff}(\omega)$ on the positive ω-axis in terms of Hermite functions, which are defined to be the product of an unnormalized Gaussian, $\mathrm{Ga}(x) \equiv \exp(-x^2/2)$, and $\mathrm{He}_k(x)$, the Hermite polynomial of degree k:

$$\tilde{C}_{ff}(\omega)\mathrm{H}(\omega) = \frac{\sqrt{2\pi}}{\tilde{\sigma}_c} \mathrm{Ga}\left(\frac{\omega - \tilde{\omega}_c}{\tilde{\sigma}_c}\right) \sum_{k=0}^{\infty} a_k \mathrm{He}_k\left(\frac{\omega - \tilde{\omega}_c}{\tilde{\sigma}_c}\right). \qquad (15)$$

Here $\mathrm{H}(\omega)$ is the Heaviside step function, $\tilde{\omega}_c$ is a frequency location parameter, and $\tilde{\sigma}_c$ is a bandwidth scale parameter. The Hermite polynomials can be generated by differentiation of the Gaussian function,

$$\mathrm{He}_k(x) = e^{x^2/2}(-1)^k \frac{d^k}{dx^k} \mathrm{Ga}(x) = k! \sum_{j=0}^{(k/2)} \frac{(-1/2)^j x^{k-2j}}{j!(k-2j)!}, \qquad (16)$$

where $(k/2)$ is the largest integer less than or equal to $k/2$. The Hermite polynomials are complete on the interval $(-\infty, \infty)$ and orthogonal with respect to the Gaussian weight; additional properties needed for our purposes are summarized in Appendix B. The coefficients in (15) are real and may be written in terms of spectral moments of $\tilde{C}_{ff}(\omega)$

Downloaded from https://academic.oup.com/gji/article/111/2/363/753853 by guest on 25 August 2022

(Rietz 1971):

$$a_k = \frac{1}{2\pi k!}\int_0^\infty \tilde{C}_{ff}(\omega)\,\mathrm{He}_k\left(\frac{\omega-\bar{\omega}_c}{\tilde{\sigma}_c}\right)d\omega$$
$$= \frac{1}{2\pi}\sum_{j=0}^{(k/2)}\frac{(-1/2)^j\hat{\mu}_{k-2j}(\bar{\omega}_c)}{j!\,(k-2j)!}, \qquad (17)$$

where $\hat{\mu}_p(\bar{\omega}_c)$ is the pth normalized, one-sided moment of $\tilde{C}_{ff}(\omega)$ about $\bar{\omega}_c$,

$$\hat{\mu}_p(\bar{\omega}_c) = \frac{1}{\tilde{\sigma}_c^p}\int_0^\infty \tilde{C}_{ff}(\omega)(\omega-\bar{\omega}_c)^p\,d\omega. \qquad (18)$$

The coefficient of the leading term, $a_0 = \hat{\mu}_0/2\pi$, is thus the total power in the isolation filter, which equals the value of its autocorrelagram at zero lag. It will be convenient to normalize the amplitude-scale of the seismograms such that this peak value is unity: $a_0 = 1$. Moreover, it will be judicious to fix the location parameter $\bar{\omega}_c$ at the centroid of the spectrum $\tilde{C}_{ff}(\omega)$ and the scale parameter $\tilde{\sigma}_c$ at its half-width; i.e. $\tilde{\sigma}_c\hat{\mu}_1(0)/\bar{\omega}_c = \hat{\mu}_2(\bar{\omega}_c) = 1$. With these choices, $a_1 = a_2 = 0$, and the zeroth-order term of (15) is the best Gaussian representation of $\tilde{C}_{ff}(\omega)$; the first correction term, measuring the skewness of the spectral peak, is third order. The notation employed in our discussion of the *Sa* isolation filters conforms to these definitions, and the values of the spectral parameters we obtained ($\bar{\omega}_c/2\pi = 28.4$ mHz and $\tilde{\sigma}_c/2\pi = 8.1$ mHz for the *SH* component) are fairly typical of body waves recorded on long-period GDSN instruments after low-pass filtering.

In the statistics literature, an expansion of a probability density in Hermite functions is known as a Gram–Charlier series (Jackson 1961; Rietz 1971). When the normalization and expansion parameters have been chosen such that $a_0 = 1$ and $a_1 = a_2 = 0$, we shall say the Gram–Charlier expansion is in its canonical form. For the case at hand, all of the coefficients given by (17) are real, so requiring the Gram–Charlier series to be in canonical form determines three quantities: the amplitude scale factor and the two spectral parameters $\bar{\omega}_c$ and $\tilde{\sigma}_c$. It is worth noting for later application that the expansion coefficients a_k for an arbitrary spectrum $S(\omega)$ are complex and, hence, six equations must be satisfied to put the series into canonical form. This system of non-linear equations determines the six-parameter Gaussian wavelet which has the same low-order ($p \le 2$) spectral moments as $S(\omega)$.

The advantage of representing $\tilde{C}_{ff}(\omega)$ as a canonical Gram–Charlier series is evident in its time-domain image. The simple Fourier-transform properties of Hermite polynomials (Hille 1926) yield

$$\tilde{C}_{ff}(t) = \mathrm{Ga}\,(\tilde{\sigma}_c t)\sum_{k=0}^{\infty} a_k(\tilde{\sigma}_c t)^k \cos\left(\bar{\omega}_c t + k\frac{\pi}{2}\right)$$
$$= \mathrm{Ga}\,(\tilde{\sigma}_c t)[\cos(\bar{\omega}_c t) + a_3(\tilde{\sigma}_c t)^3 \sin(\bar{\omega}_c t)$$
$$+ a_4(\tilde{\sigma}_c t)^4 \cos(\bar{\omega}_c t) - \cdots]. \qquad (19)$$

The leading term is a Gaussian wavelet with a carrier frequency $\bar{\omega}_c$ and an envelope half-width equal to the inverse of the spectral half-width $\tilde{\sigma}_c$. The first correction term is third order, containing the same carrier wave, but phase-shifted by $3\pi/2$ and modulated by an additional factor proportional to t^3. The factor of t^k in the kth-order term implies the existence of a finite neighbourhood in the vicinity of the peak of the autocorrelagram where the error associated with the Gaussian-wavelet approximation can be made arbitrarily small. This asymptotic behaviour carries over to the other correlagrams considered in this paper and is the theoretical keystone of our methodology.

Of course, it is always possible to eliminate the higher order coefficients in (19) by pre-filtering the isolation filter so that $\tilde{C}_{ff}(\omega)$ has the form of the Gaussian pre-multiplier in (15). This spectrum is a real, even function with peaks at $\pm\bar{\omega}_c$. Enforcing the Gaussian-wavelet approximation by spectral shaping requires the relative bandwidth

$$\xi_0 = \tilde{\sigma}_c/\bar{\omega}_c \qquad (20)$$

to be sufficiently small that the contribution of the peak centred at $-\bar{\omega}_c$ to the second-moment integral (18) can be neglected; i.e.

$$\frac{\sqrt{2\pi}}{\tilde{\sigma}_c^3}\int_0^\infty \mathrm{Ga}\left(\frac{\omega+\bar{\omega}_c}{\tilde{\sigma}_c}\right)(\omega-\bar{\omega}_c)^2\,d\omega \sim \frac{2\sqrt{\pi}\,e^{-1/\xi_0^2}}{\xi_0} \ll 1. \qquad (21)$$

ξ_0 will be called the pre-filtering parameter; it is the first of a several 'control variables' at our disposal to insure the Gaussian-wavelet approximation is valid (see Table 1). In our applications, the inequality in (21) is always satisfied; in the *Sa* example, $\xi_0 = 0.29$, and the asymptotic expression for the integral yields a value on the order of 10^{-5}. In fact, the low-passed GDSN waveforms from intermediate-magnitude earthquakes usually have peaked power spectra with nearly Gaussian shapes, so that a Gaussian wavelet accurately describes the autocorrelagram over a significant fraction of the envelope half-width $\tilde{\sigma}_c^{-1}$ without any fancy pre-filtering. Fig. 8 compares the normalized autocorrelagram for the *SH*-component isolation filter used in our analysis of the *Sa* phase (solid line) with the Gram–Charlier partial sums through fourth order (dashed lines). The second-order (Gaussian) approximation yields a residual of less than 1 per cent within $\pm\tilde{\sigma}_c^{-1} = 20$ s of the peak, and less than 10 per cent within ± 100 s. The coefficient a_3 is only 0.03, so the third-order term is down by nearly two orders of magnitude.

In the case of the autocorrelagram, both the carrier and the envelope of the Gaussian wavelet are centred at zero lag. We seek to describe the Gaussian-wavelet approximations to much more complex functions; specifically, the cross-correlagrams (5) and (8), where the spectral parameters have been modified by windowing, filtering and attenuation, and time shifts have been introduced by

Table 1. Control parameters and their values.

			SH	*PSV*
ξ_0	$\frac{\tilde{\sigma}_c}{\bar{\omega}_c}$	pre-filtering	0.3	0.3
ξ_1	$\frac{\tilde{\sigma}_c}{\tilde{\sigma}_{wc}}$	time-localization	0.9	0.8
ξ_2	$\frac{\sigma_i'}{\tilde{\sigma}_{wc}}$	frequency-localization	0.1 – 0.4	0.1 – 0.4
ξ_3	$\frac{\omega_i' - \bar{\omega}_c}{\tilde{\sigma}_{wc}}$	frequency-shift	(−1.9) – 1.5	(−2.1) – 1.5
ξ_4	$\sqrt{\frac{\tilde{\sigma}_f^2}{\tilde{\sigma}_f^2+\gamma^2}}$	weighting function	0.2	0.2

Downloaded from https://academic.oup.com/gji/article/111/2/363/753853 by guest on 25 August 2022

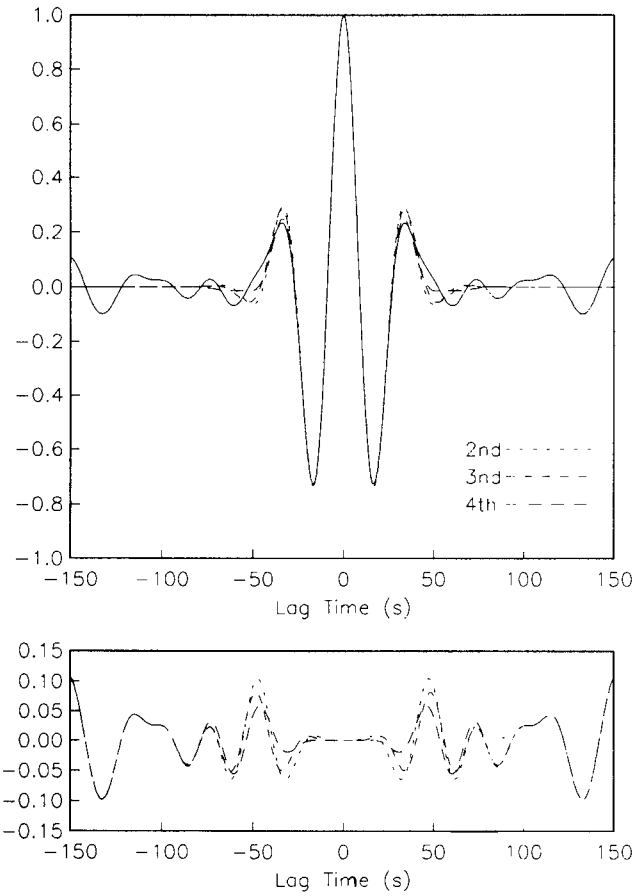

Figure 8. $\tilde{C}_{ff}(t)$ (solid line) for the transverse-component isolation filter of *Sa*. The dashed lines represent partial sums of the Gram–Charlier series; the residuals are plotted below on an expanded scale.

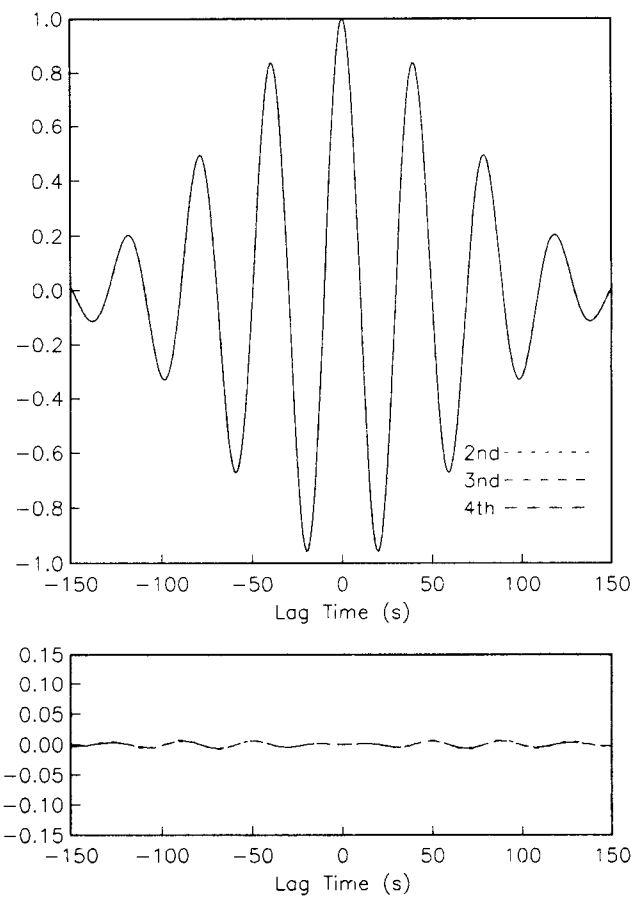

Figure 9. $F_i W\tilde{C}_{ff}(t)$ (solid line) for the transverse-component isolation filter of *Sa*. The dashed lines represent partial sums of the Gram–Charlier series; the residuals are plotted below on an expanded scale.

interference and dispersion. The convenient properties of Gram–Charlier series allow us to derive explicit expressions for the parameters of these Gaussian wavelets, as well as the higher order correction terms needed to validate the Gaussian approximation. Aspects of an operational calculus we have developed for this purpose are described in Appendix C.

4.2 Gaussian wavelet approximation of the filtered, windowed autocorrelagram

The first operation to be considered is windowing, which localizes the broad-band correlagram in the lag-time domain. Windowing reduces (though it does not eliminate) the contributions of interfering wave groups to the observations. We assume that the window $W(t)$ is a real-valued, one-sided, even function centred at a lag-time t_w. Then, the time-domain image of its canonical Gram–Charlier expansion can be written as a series in even powers of t:

$$W(t) = \mathrm{Ga}\,[\sigma_w(t - t_w)]\{1 + b_4[\sigma_w(t - t_w)]^4 - b_6[\sigma_w(t - t_w)]^6 + \cdots\}, \tag{22}$$

where σ_w is the half-width of its Fourier spectrum $W(\omega)$.

The coefficients are given by the spectral integrals

$$b_k = \frac{1}{\pi k!}\int_0^\infty W(\omega)\,\mathrm{He}_k\left(\frac{\omega}{\sigma_w}\right)d\omega, \tag{23}$$

where we have chosen to represent $W(\omega)$ in terms of Hermite expansion on $(-\infty, \infty)$ centred at $\omega = 0$. In the *Sa* example, the window we applied was a Hanning taper of total length $T_w = 140$ s, for which $\sigma_w/2\pi = 5.2$ mHz and $b_4 = 0.01$.

To form $W\tilde{C}_{ff}(t)$, we centre the taper on the peak of the autocorrelation function ($t_w = 0$) and multiply. The theorems in Appendix C yield

$$W\tilde{C}_{ff}(t) = \mathrm{Ga}\,(\tilde{\sigma}_{wc}t)\sum_{k=0}^{\infty} c_k(\tilde{\sigma}_{wc}t)^k \cos\left(\tilde{\omega}_c t + k\frac{\pi}{2}\right), \tag{24}$$

where the new half-width $\tilde{\sigma}_{wc} \equiv \sqrt{\sigma_w^2 + \tilde{\sigma}_c^2}$ reflects the spectral broadening due to the time-domain localization. The kth coefficient is given by the convolutional sum

$$c_k = \sum_{n=0}^{k} a_n b_{k-n}\xi_1^n(1 - \xi_1^2)^{(k-n)/2}, \tag{25}$$

$$\xi_1 \equiv \tilde{\sigma}_c/\tilde{\sigma}_{wc}. \tag{26}$$

The first four are: $c_0 = 1$, $c_1 = c_2 = 0$, $c_3 = \xi_1^3 a_3$, and $c_4 = \xi_1^4 a_4 + (1 - \xi_1^2)^2 b_4$.

Downloaded from https://academic.oup.com/gji/article/111/2/363/753853 by guest on 25 August 2022

The dimensionless parameter ξ_1 measures the degree of time localization achieved by windowing. If the window is wide, $\sigma_w \ll \bar{\sigma}_c$, $\xi_1 \approx 1$, and $c_k \approx a_k$; if it is narrow, $\sigma_w \gg \bar{\sigma}_c$, $\xi_1 \approx 0$, and $c_k \approx b_k$. Since, according to (19), the higher order coefficients $\{a_k : k \geq 3\}$ contribute more to the autocorrelagram at lag-times far from its peak, the time-localization parameter ξ_1 can be employed as a second control variable for regulating non-Gaussian terms in the spectrum. For the Hanning taper employed in the *Sa* example, we have used $\xi_1 = 0.84$, so that widowing reduces the third-order coefficient by about 40 per cent.

The next operation to consider is the narrow-band filtering which localizes the windowed autocorrelagram in the frequency domain: $F_i W\tilde{C}_{ff}(t) \equiv F_i(t) * [W(t)\tilde{C}_{ff}(t)]$. The index i specifies a filter F_i with half-bandwidth σ_i and centre frequency ω_i. For our analysis of GDSN records, we typically use a series five to ten filters centred at frequencies from 10 to 45 mHz, each with $\sigma_i/\omega_i \approx 0.1$. Although we have worked out complete expressions involving filters with arbitrary Gram–Charlier coefficients, the analysis in this paper is simplified by considering only zero-phase Gaussian filters. In practice, we have found that the non-Gaussian structure introduced by any reasonable zero-phase filter—e.g., windowing the spectrum with a narrow Hanning taper centred at ω_i—is negligible.

In the special case when $W\tilde{C}_{ff}(t)$ can be approximated a simple Gaussian wavelet (i.e. $c_k = 0$ for $k \geq 1$), its spectrum can be analytically multiplied with an appropriately normalized Gaussian filter and Fourier transformed to obtain $F_i W\tilde{C}_{ff}(t) = \mathrm{Ga}(\sigma_i' t)\cos(\omega_i' t)$, where ω_i' and σ_i' are the effective centre frequency and half-bandwidth resulting from the windowing and filtering:

$$\omega_i' = \frac{\bar{\sigma}_{wc}^2 \omega_i + \sigma_i^2 \bar{\omega}_c}{\bar{\sigma}_{wc}^2 + \sigma_i^2}, \tag{27}$$

$$\sigma_i'^2 = \frac{\bar{\sigma}_{wc}^2 \sigma_i^2}{\bar{\sigma}_{wc}^2 + \sigma_i^2}. \tag{28}$$

Retaining these values as expansion parameters when $c_k \neq 0$, we can apply the theorems of Appendix C to obtain the general expression

$$F_i W\tilde{C}_{ff}(t) = \mathrm{Ga}(\sigma_i' t) \sum_{k=0}^{\infty} d_k (\sigma_i' t)^k \cos\left(\omega_i' t + k\frac{\pi}{2}\right), \tag{29}$$

where the Gram–Charlier coefficients are given by a double infinite sum over the $\{c_k\}$:

$$d_k = \xi_2^k \sum_{j=0}^{\infty} \left(\frac{-1}{2}\right)^j (1-\xi_2^2)^j \sum_{l=0}^{\infty} \frac{(2j+k+l)!}{j!k!l!} \xi_3^l c_{2j+k+l}. \tag{30}$$

Here we have introduced two new control variables, a frequency-localization parameter,

$$\xi_2 = \sigma_i'/\bar{\sigma}_{wc}, \tag{31}$$

and a frequency-shift parameter,

$$\xi_3 = \frac{\omega_i' - \bar{\omega}_c}{\bar{\sigma}_{wc}}. \tag{32}$$

Expansion (29) is not in canonical form, since the terms proportional to c_n contribute to the d_k for all $k \leq n$, so that $d_0 \neq 1$, $d_1 \neq d_2 \neq 0$. The leading terms for the first five coefficients are

$$d_0 = 1 + [\xi_3^3 - 3\xi_3(1-\xi_2^2)]c_3 + [\xi_3^4 - 6\xi_3^2(1-\xi_2^2) + 3(1-\xi_2^2)^2]c_4 + \cdots, \tag{33a}$$

$$d_1 = \xi_2\{3[\xi_3^2 - (1-\xi_2^2)]c_3 + 4[\xi_3^3 - 3\xi_3(1-\xi_2^2)]c_4 + \cdots\}, \tag{33b}$$

$$d_2 = \xi_2^2\{3\xi_3 c_3 + 6[\xi_3^2 - (1-\xi_2^2)]c_4 + \cdots\}, \tag{33c}$$

$$d_3 = \xi_2^3(c_3 + 4\xi_3 c_4 + \cdots), \tag{33d}$$

$$d_4 = \xi_2^4(c_4 + \cdots). \tag{33e}$$

When the bandwidth reduction due to the filtering is large ($\xi_2 \ll 1$), the centre frequency and half-bandwidth of $F_i W\tilde{C}_{ff}(\omega)$ approach the values of the applied filter. Since the contribution of the kth term is attenuated by the factor $(\xi_2)^k$, this frequency-localization parameter can be employed to control the Gaussian-wavelet approximation. In the *Sa* example, values of ξ_2 that we used ranged from 0.11 at 10 mHz to 0.44 at 45 mHz.

The frequency-shift parameter ξ_3 measures, in units of $\bar{\sigma}_{wc}$, the position of the applied filter relative to the centre frequency of windowed correlagram. The contribution of c_n to d_k scales as $|\xi_3|^{n-k}$; hence, the Gaussian-wavelet approximation can also be improved by choosing values of ω_i near $\bar{\omega}_c$. If the higher order terms in the windowed correlagram are appreciable, then the approximation will fail towards the edges of the pass-band where $|\xi_3|$ becomes large. In practice, the limiting factor on the useable bandwidth of the data is not typically this kind of theoretical breakdown, but rather the decrease in the effective signal-to-noise ratio; i.e. the signal suppression described by the first Gaussian pre-multiplier in (29).

The approximation realized by the actual computational procedure is, in fact, better than the Gaussian wavelet obtained from the zeroth-order term in (29). Instead of fixing ω_i' and σ_i' at the theoretical values specified by (27) and (28), we estimate them numerically using the least-squares procedure described in the previous section. That is, we normalize the cross-correlagram to unit amplitude at $t = 0$ and then determine a centre frequency $\bar{\omega}_f$ and half-bandwidth $\bar{\sigma}_f$ from the approximation

$$F_i W\tilde{C}_{ff}(t) \approx \bar{g}(t) \equiv \mathrm{Ga}(\bar{\sigma}_f t)\cos(\bar{\omega}_f t), \tag{34}$$

by minimizing a χ^2 quadratic form analogous to (7). Because the squared differences between $F_i W\tilde{C}_{ff}(t)$ and $\bar{g}(t)$ are weighted by a Gaussian factor $\exp(-\gamma^2 t^2)$, this procedure requires the fit to be best near $t = 0$, where, according to (29), the contributions of the higher order terms vanish. Hence, the minimum will be achieved when the low-order moments of the spectrum $\bar{g}(\omega)$ match those of $F_i W\tilde{C}_{ff}(\omega)$; i.e. when

$$\bar{\omega}_f = \omega_i' + \sigma_i' d_1/d_0, \tag{35}$$

$$\bar{\sigma}_f^2 = \sigma_i'^2[1 - (d_1/d_0)^2 + 2d_2/d_0]. \tag{36}$$

The correction terms are usually very small, however, so that the numerical deviations of the Gaussian parameters from (27) and (28) are practically negligible. The worst case in the *Sa* example occurs at $\omega_i/2\pi = 45$ mHz. Here ξ_2 and ξ_3 are largest (0.43 and 1.5, respectively), but the deviations are less than 1 per cent in centre frequency and 2 per cent in bandwidth.

Downloaded from https://academic.oup.com/gji/article/111/2/363/753853 by guest on 25 August 2022

In any case, the filtered, windowed autocorrelagram can always be written in the cannonical form

$$F_i W\tilde{C}_{ff}(t) = \mathrm{Ga}\,(\tilde{\sigma}_f t)\Big[\cos(\tilde{\omega}_f t) + \sum_{k=3}^{\infty} \tilde{d}_k (\tilde{\sigma}_f t)^k \cos\left(\tilde{\omega}_f t + k\frac{\pi}{2}\right)\Big]. \quad (37)$$

compares the filtered, windowed autocorrelation function (solid line) with the Gram-Charlier partial sums through fourth order (dashed lines).

Fig. 9 shows the fit of equation (37) to the filtered, windowed autocorrelagram through the fourth order term.

The quadratic error χ^2 incurred by fitting a Gaussian wavelet to $F_i W\tilde{C}_{ff}(t)$ can be integrated term-by-term. The results of a complete analysis, in which we employ some inconsequential approximations, are

$$\chi^2 = \sum_{k=6}^{\infty} e_k \,\mathrm{He}_k(0), \quad (38)$$

$$e_k = \left(\frac{\xi_4}{2}\right)^k \sum_{n=1}^{k} (-1)^{k-n} \tilde{d}_n \tilde{d}_{k-n}, \quad (39)$$

where the size of the coefficients is governed by a new control variable, the weighting-function parameter

$$\xi_4 = \sqrt{\frac{\tilde{\sigma}_f^2}{\tilde{\sigma}_f^2 + \gamma^2}}. \quad (40)$$

$\mathrm{He}_k(0)$ is identically zero for all odd values of k, and both $\tilde{d}_1$ and $\tilde{d}_2$ are zero by construction; hence, $e_k = 0$ for $k \le 5$, which is why the first non-zero term in (38) is sixth order. Assuming this leading term dominates, we obtain a dimensionless measure of the rms error incurred by truncating the higher order terms in (37):

$$|\chi| \approx \sqrt{15}\xi_1^3\xi_2 |a_3 + 4\xi_1\xi_3 a_4| \left(\frac{\xi_4}{2}\right)^3. \quad (41)$$

The Gaussian-wavelet approximation will be strictly valid when $|\chi| \ll 1$. The worst case in the *Sa* example occurs for the filter frequency at the high end of the band (45 mHz), where the truncation error for the autocorrelagram is estimated to be $|\chi| \approx 0.018|a_3 + 6.2a_4| \approx 0.004$. A similar value applies to the cross-correlagrams, as confirmed by the excellent Gaussian-wavelet approximations displayed in Fig. 5(c). In our processing, we typically take $\xi_4 = 1/\sqrt{2}$, so that the last factor in (41) alone damps the truncation error by over an order of magnitude. In cases where the non-Gaussian coefficients $\{a_k : k \ge 3\}$ are larger, it is possible, if necessary, to decrease ξ_4 further without appreciably degrading our ability to estimate the wavelet parameters. Suppression of the truncation error can also be achieved by decreasing the other control variables, which are summarized in Table 1. In practice, therefore, the validity of the Gaussian-wavelet approximation sets only weak limits on the domain of the theory's application, and we shall employ it throughout our subsequent derivations.

4.3 Differential propagation

The isolation filter $\tilde{f}(t)$ computed as the sum (4) over synthetic components will correspond to some waveform $f(t)$ on the observed seismogram. The spectrum of $f(t)$ can be written as the product of the spectra specifying the source excitation, the effects of propagation, and the instrument response: $f(\omega) = I(\omega)P(\omega)S(\omega)$. Since the objective of our analysis is to investigate the earth structure by placing constraints on the propagation operator P, we shall assume both S and I are exactly known and have been included in the calculation of $\tilde{f}(\omega)$. Then,

$$f(\omega) = D(\omega)\tilde{f}(\omega), \quad (42)$$

where $D(\omega) = P(\omega)/\tilde{P}(\omega)$ is the differential propagation operator. This operator can be written in its exponential form $D(\omega) = e^{i\delta k(\omega)x}$, where x is the propagation distance and $\delta k(\omega) \equiv k(\omega) - \tilde{k}(\omega)$ is the complex-valued differential wavenumber. The differential wavenumber can be expanded in a Taylor series about an arbitrary frequency ω_0:

$$\delta k(\omega) = \delta k(\omega_0) + (\omega - \omega_0)\delta\dot{k}(\omega_0) + \tfrac{1}{2}(\omega - \omega_0)^2 \delta\ddot{k}(\omega_0) + \cdots. \quad (43)$$

Most methods for measuring the differential dispersion of surface waves (e.g. Dziewonski *et al.* 1972) assume the effective bandwidth is small enough that (43) can be truncated after the linear term. This is usually adequate, although in cases where the dispersion is strong and the earth model used to compute the synthetics is a poor representation of structure along the path, the linear-dispersion approximation sometimes fails. It is possible to include completely the quadratic-dispersion terms in the GSDF theory by introducing a carrier-phase term proportional to t^2, yielding a six-parameter Gaussian wavelet; we have derived and implemented the quadratic expressions in a version of our analysis codes. For most applications to long-period seismograms, however, a first-order approximation is completely adequate. We therefore confine our detailed discussion to the first two terms of (43). For completeness, the equations involving the second-order terms are given in Appendix D.

The linear approximation to the differential propagation operator can be parametrized by four real-valued, time-like quantities:

$$D(\omega) \cong \exp\{-\omega_0\,\delta\tau_q(\omega_0) - (\omega - \omega_0)\,\delta\tau_a(\omega_0) + i[\omega_0\,\delta\tau_p(\omega_0) + (\omega - \omega_0)\,\delta\tau_g(\omega_0)]\}. \quad (44)$$

The imaginary part of the exponential argument defines the differential phase delay $\delta\tau_p$ and the differential group delay $\delta\tau_g$ at ω_0:

$$\delta\tau_p(\omega_0) \equiv x\frac{\mathcal{R}e\,\{\delta k(\omega_0)\}}{\omega_0} = \tau_p(\omega_0) - \tilde{\tau}_p(\omega_0), \quad (45)$$

$$\delta\tau_g(\omega_0) \equiv x\,\mathcal{R}e\,\{\delta\dot{k}(\omega_0)\} = \tau_g(\omega_0) - \tilde{\tau}_g(\omega_0). \quad (46)$$

τ_p and τ_g are the total phase and group delays of the observed waveform relative to the origin time of the event, including those due to the source excitation and instrument response, and $\tilde{\tau}_p$ and $\tilde{\tau}_g$ are the corresponding phase and group delays computed for the reference model. Under the assumption that the source and instrument are exactly modelled, (45) and (46) are identical to the differences in the phase and group traveltimes.

The real part of the exponential argument defines two differential attenuation times, $\delta\tau_q$ and $\delta\tau_a$. In the special case where the amplitude ratio $\mathcal{R}e\,[f(\omega)/\tilde{f}(\omega)]$ is primarily controlled by the difference in a frequency-independent

Downloaded from https://academic.oup.com/gji/article/111/2/363/753853 by guest on 25 August 2022

attenuation factor Q^{-1}, we can write

$$\delta\tau_q(\omega_0) \equiv x \frac{\mathcal{I}m\{\delta k(\omega_0)\}}{\omega_0} \cong \frac{1}{2}\tilde{\tau}_p(\omega_0)[Q^{-1} - \bar{Q}^{-1}], \quad (47)$$

$$\delta\tau_a(\omega_0) \equiv x\,\mathcal{I}m\{\delta\dot{k}(\omega_0)\} \cong \frac{1}{2}\tilde{\tau}_g(\omega_0)[Q^{-1} - \bar{Q}^{-1}]. \quad (48)$$

This particular relationship between the amplitude parameters and the differential attenuation ignores terms of order Q^{-2}. When the absolute dispersion is small in the sense that $\bar{\sigma}_c|\tilde{\tau}_p - \tilde{\tau}_g| \ll 1$, then the first-order approximation implies $\delta\tau_q = \delta\tau_a$, and the time corresponds to a differential form of the t^* parameter commonly used in the analysis of body waves (e.g. Burdick 1978). This identification is avoided in this paper, because we want to allow for more complex amplitude effects, including frequency-dependent attenuation, amplitude perturbations associated with differential focussing and reflection, and interference effects owing to differential phase shifts among the various waveforms involved in (4). In modelling these effects, the two amplitude parameters are allowed to vary separately.

The spectrum of the cross-correlagram is, by definition, $C_{ff}(\omega) = D(\omega)\tilde{C}_{ff}(\omega)$. A first-order approximation to its Gram–Charlier series can be obtained by evaluating (44) at $\omega_0 = \bar{\omega}_c$ and multiplying it into (15). We can reduce this series to canonical form and Fourier transform the results to get the time-domain expansion.

$$C_{ff}(t) = \exp(-\bar{\omega}_c\,\delta\tau_q)\,\mathrm{Ga}[\sigma_c(t-\delta\tau_g)]\left\{\cos[\omega_c(t-\delta\tau_p)] + \sum_{k=3}^{\infty} a'_k[\sigma_c(t-\delta\tau_g)]^k \cos\left[\omega_c(t-\delta\tau_p) + \frac{k\pi}{2}\right]\right\} + O(\varepsilon^2), \quad (49)$$

where $\{\delta\tau_x = \delta\tau_x(\bar{\omega}_c) : x = q, p, a, g\}$ and ε is a dimensionless parameter that measures the magnitude of the differential dispersion. In deriving (49) we have specificially assumed that the differential phase and amplitude variations across the bandwidth are first order in the sense that $\bar{\sigma}_c|\delta\tau_p - \delta\tau_g| \sim \bar{\sigma}_c\,\delta\tau_a \sim 2\pi\varepsilon$. It is important to note that no constraint is placed on the size of $\delta\tau_q$, which sets only a frequency-independent amplitude scale, nor on the non-dispersive part of the differential traveltime, $(\delta\tau_p + \delta\tau_g)/2$. The latter need not be small because it can be factored out of (49) and treated, via the Fourier shift theorem, as a simple displacement of $f(t)$ relative to $\bar{f}(t)$.

Equation (49) shows that, to first order in ε, the Gaussian envelope of the Gram–Charlier series is shifted by the differential group delay $\delta\tau_g(\bar{\omega}_c)$ and its cosine carrier is shifted by the differential phase delay $\delta\tau_p(\bar{\omega}_c)$. The first-order expressions for the perturbed carrier frequency and half-bandwidth are

$$\omega_c \cong \bar{\omega}_c - \bar{\sigma}_c^2\,\delta\tau_a(\bar{\omega}_c), \quad (50)$$

$$\sigma_c \cong \bar{\sigma}_c - 3\bar{\sigma}_c^2\,\delta\tau_a(\bar{\omega}_c)a_3, \quad (51)$$

and the higher order coefficients in (49) are related to those of $\tilde{C}_{ff}$ by

$$a'_k = \sum_{j=0}^{\infty}\binom{k+j}{j}[-\bar{\sigma}_c\,\delta\tau_a(\bar{\omega}_c)]^j a_{k+j} \cong a_k - (k+1)\bar{\sigma}_c\,\delta\tau_a(\bar{\omega}_c)a_{k+1} \quad (k \geq 3). \quad (52)$$

The perturbations in the last three expressions are due entirely to the frequency dependence of the differential amplitude, which is generally weak. For example, if the observed Qs for the *Sa* phases of Fig. 4 were a factor of two lower than the model values (~200)—a fairly extreme example—then $|\delta\tau_a| \approx 5$ s. In this case, the differential attenuation would induce a carrier-frequency shift of about −1.4 mHz, which is greater than the frequency estimation errors and thus potentially observable. The difference in the half-bandwidths would be less than 0.2 mHz, however, a completely negligible perturbation in terms of its effect on the signal structure. In practice, assuming $\sigma_c = \bar{\sigma}_c$ is usually an excellent approximation, since the bandwidth difference is proportional to the skewness coefficient a_3, which is generally small. This approximation, which also depends on the quadratic terms in the differential dispersion being negligible, is necessary to limit the number of GSDFs to four.

We therefore consider the Gaussian wavelet

$$C_{ff}(t) = \exp(-\bar{\omega}_c\,\delta\tau_q)\,\mathrm{Ga}[\bar{\sigma}_c(t-\delta\tau_g)] \times \cos[(\bar{\omega}_c - \bar{\sigma}_c^2\,\delta\tau_a)(t-\delta\tau_p)]. \quad (53)$$

The four differential time parameters in (53) correspond exactly to the GSDFs defined in (9)–(12). In other words, fitting Gaussian wavelets to $C_{ff}(t)$ yields, to first order in ε, $\delta t_x(\bar{\omega}_c) = \delta\tau_x(\bar{\omega}_c)$ for $x \in \{q, p, a, g\}$. Fig. 10 illustrates in graphical form how each of the four parameters perturbs a narrow-band ($\xi_0 = 0.1$) correlagram.

Equation (53) provides an inadequate basis for the analysis of broad-band data, however. The approximations employed in its derivation can always be enforced by pre-filtering the seismograms, of course, but this tactic has the undesirable consequence of spreading out energy in the time domain, thereby increasing the interference with signals not included in the isolation filter. To take full

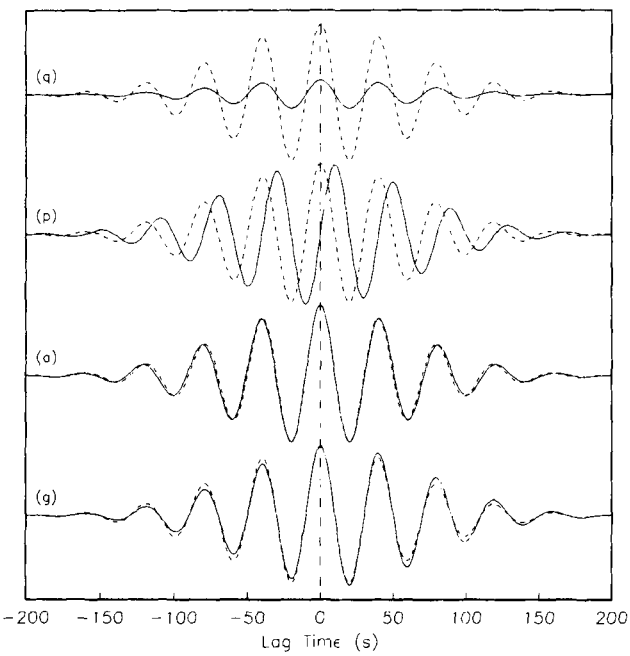

Figure 10. Illustration of the effect of the generalized data functionals on the cross-correlation function, $C_{ff}(t)$ (solid line), for a 10 s perturbation to $\delta\tau_x$ compared with $\tilde{C}_{ff}(t)$ (dashed line).

Downloaded from https://academic.oup.com/gji/article/111/2/363/753853 by guest on 25 August 2022

advantage of the available bandwidth, it is necessary to localize the correlagrams by windowing in the time domain prior to narrow-band filtering in the frequency domain. We first investigate the effect of these sequential operations on the GSDFs by continuing with the detailed analysis of an isolated waveform. An explicit consideration of interference effects will be deferred to Section 4.5.

4.4 Cross-correlagram of an isolated waveform

A Gaussian-wavelet approximation to the filtered, windowed cross-correlagram $F_iWC_{ff}(t) = F_i(t) * W(t)[\bar{f}(t) \otimes f(t)]$ will yield an approximate description of $F_iWC_{fs}(t)$ when the windowing is effective in isolating $f(t)$ from other phases on the seismogram. As in (22), $W(t)$ is assumed to be symmetrical function with a half-width σ_w^{-1}. In order to minimize the signal distortion by the window, we centre $W(t)$ at the peak of the cross-correlagram, which occurs at some lag-time t_c. Differentiating (53) gives the location of this peak, correct to $O(\varepsilon)$:

$$t_c \cong \frac{\delta\tau_p(\bar{\omega}_c) + 2\pi n/\bar{\omega}_c + \xi_0^2\,\delta\tau_g(\bar{\omega}_c)}{1+\xi_0^2}, \tag{54a}$$

$$n = \left\{\frac{1}{2\pi}\,\bar{\omega}_c[\delta\tau_g(\bar{\omega}_c) - \delta\tau_p(\bar{\omega}_c)] + \frac{1}{2}\right\}. \tag{54b}$$

The brackets in (54b) denote the largest integer less than or equal to the argument. The integer n describes the cycle-skipping which occurs whenever the dispersion is strong enough that the envelope peak is displaced by more than a half-period away from the carrier's zero-phase point. When the relative bandwidth ξ_0 is small, the envelope decays slowly and t_c approaches $\delta\tau_p + 2n\pi/\bar{\omega}_c$; i.e. the shift of the cross-correlation peak away from zero lag measures the differential phase delay at $\bar{\omega}_c$ to within the n-cycle ambiguity. As ξ_0 increases, the envelope rolls off more rapidly, and the peak time is biased towards the differential group delay. These properties are useful for the interpretation of ordinary traveltimes derived by cross-correlation methods (Jordan 1980; Sipkin & Jordan 1980).

We filter the windowed cross-correlagram and fit it with a five-parameter Gaussian wavelet by minimizing a χ^2 quadratic form like (7):

$$F_iWC_{ff}(t) \approx g(t) \equiv A\ \mathrm{Ga}\,[\sigma_f(t-t_g)]\cos[\omega_f(t-t_p)]. \tag{55}$$

For each narrow-band filter F_i, we compute $\{\delta t_x = \delta t_x(\bar{\omega}_f) : x = \mathrm{p, g, q, a}\}$ by combining the cross-correlagram parameters $\{A, \omega_f, \sigma_f, t_p, t_g\}$ with the autocorrelagram parameters $\{\bar{A}=1, \bar{\omega}_f, \bar{\sigma}_f, \bar{t}_p = \bar{t}_g = 0\}$ using equations analogous to (9)–(12). These differential time measurements can be related to the dispersion parameters defined in (44) through the Gram–Charlier coefficients $\{d_k'\}$ for $F_iWC_{ff}(t)$ derived using the equations in Appendix B. The resulting series will not be in canonical form, but we can always choose the control variables to make the deviations $(1-d_0')$, d_1' and d_2' as small as we like (*cf.* equations 33a–c). In particular, we may assume the control variables have been adjusted such that the deviations are $O(\varepsilon)$, which implies that $\sigma_f = \bar{\sigma}_f + O(\varepsilon^2)$. (This is certainly valid for the *Sa* example.) Because the algebra is rather heavy and the general expressions for the coefficients are unedifying, we give only the formulae for the GSDFs evaluated at $\bar{\omega}_f$, valid to $O(\varepsilon)$.

The equation for the apparent differential group delay is simple and easily interpreted:

$$\begin{aligned}\delta t_g &= \xi_1^2\,\delta\tau_g(\bar{\omega}_f) + (1-\xi_1^2)t_c \\ &= \delta\tau_g(\bar{\omega}_f) + (1-\xi_1^2)[t_c - \delta\tau_g(\bar{\omega}_f)].\end{aligned} \tag{56}$$

For a window wider than the autocorrelagram $C_{ff}(t)$, i.e. when $\xi_1 \approx 1$, the value observed through the narrow-band filter is nearly equal to the actual differential group delay evaluated at the apparent centre frequency $\bar{\omega}_f$. As the window is made narrower, δt_g approaches the centre time of the window, t_c. The parameters in the *Sa* example give a 0.29/0.71 weighting between these two limits, and the difference $\delta t_g - \delta\tau_g$, plotted as a function of frequency in Fig. 11(g), reaches about +5 s at the high end of the band. Since t_c is an observable, equation (56) can be used to correct the apparent differential group delay for this windowing bias.

Windowing also affects the apparent differential phase delay. We find

$$\delta t_p = \delta\tau_p(\bar{\omega}_f) + (1-\xi_1^2)\left(\frac{\bar{\omega}_f - \bar{\omega}_c}{\bar{\omega}_f}\right)[t_c - \delta\tau_g(\bar{\omega}_f)]. \tag{57}$$

The windowing bias is again proportional to $(1-\xi_1^2)$ but in this case it is further suppressed by the fractional shift in the centre frequency due to the filtering. Although this factor vanishes at the centre of the band, its magnitude can approach unity near the low- and high-frequency ends, and the correction can be significant (Fig. 11p).

The amplitude of $C_{ff}(\omega)$ has a frequency dependence in the vicinity of $\bar{\omega}_f$ measured by $\delta\tau_a$. The corresponding parameter for $F_iWC_{ff}(\omega)$ is

$$\delta t_a = \xi_1^2\,\delta\tau_a(\bar{\omega}_f). \tag{58}$$

Windowing therefore suppresses this differential time by the square of the time-localization parameter. In the limit of a very narrow window, the correlagrams are reduced to sharp peaks with equally flat spectra, and $\delta t_a \to 0$. Finally, the effect of the time-series operations on the amplitude ratio $\bar{\omega}_f$ is described by

$$\delta t_q = \delta\tau_q(\bar{\omega}_f) - (1-\xi_1^2)\left(\frac{\bar{\omega}_f - \bar{\omega}_c}{\bar{\omega}_f}\right)\delta\tau_a(\bar{\omega}_f). \tag{59}$$

The second term is the amplitude bias due to windowing, analogous to that in (57). Figs 11(a) and (q) show the amplitude correction terms for the *Sa* example.

4.5 Effects of interference on non-isolated waveforms

Equations (56)–(59) express the quantities actually measured, the δt_x's, in terms of the dispersion parameters more fundamentally related to earth structure, the $\delta\tau_x$'s, in the special case when the windowing is effective in eliminating the interference from waveforms on the seismogram not represented by the isolation filter. On the synthetic seismograms, this interference is measured by the four time shifts that describe the deviations of the filtered, windowed cross-correlagram $F_iW\bar{C}_{fs}$ from the autocorrelagram $F_iW\bar{C}_{ff}$: a phase delay $\tilde{t}_p$, a group delay $\tilde{t}_g$, and two amplitude

Downloaded from https://academic.oup.com/gji/article/111/2/363/753853 by guest on 25 August 2022

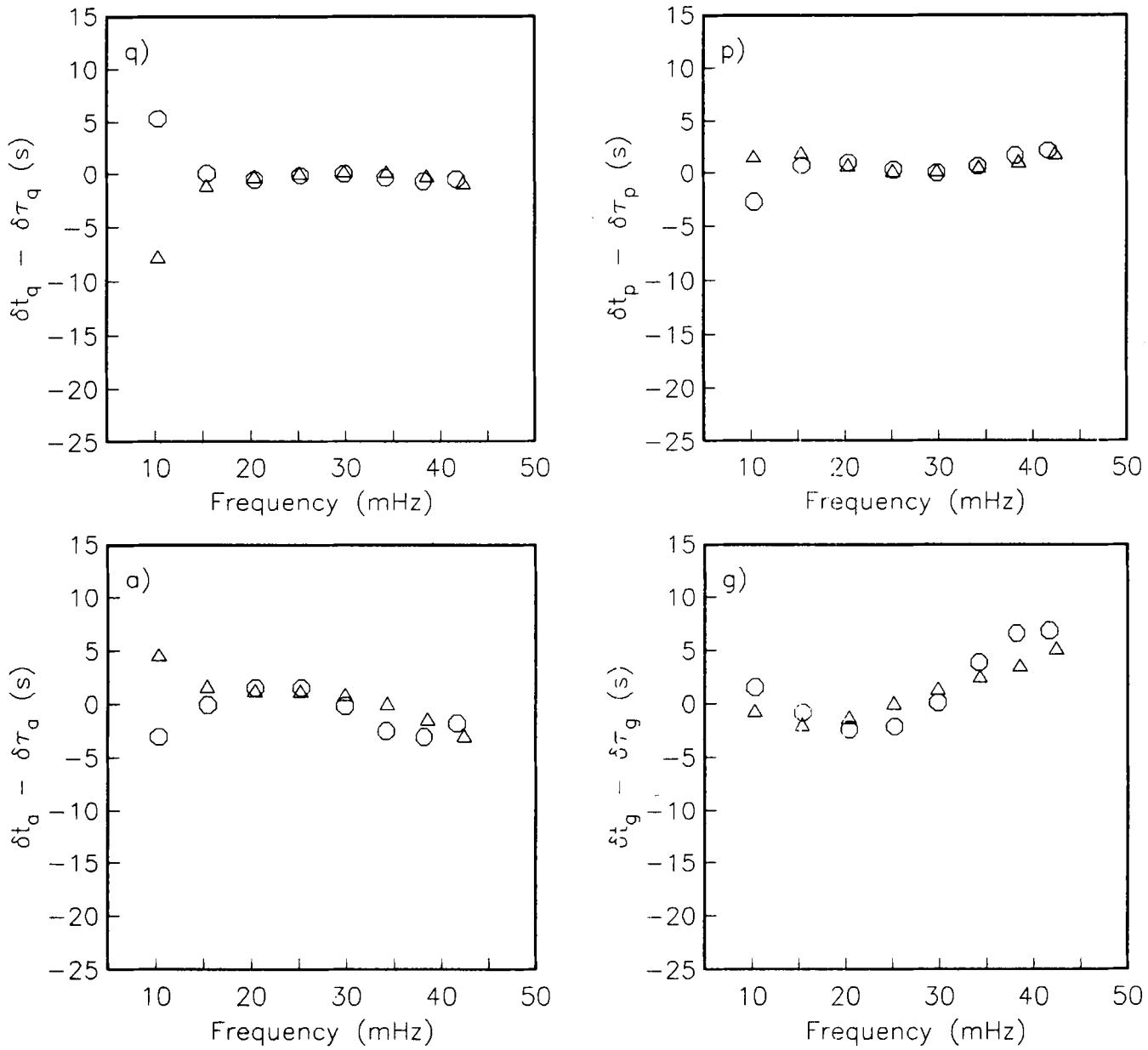

Figure 11. Correction factors for windowing and filtering ($\delta t_x - \delta\tau_x$) plotted as a function of frequency for the vertical (circles) and transverse (triangles) component generalized data functionals.

parameters

$$\tilde{t}_q = -\frac{1}{\tilde{\omega}_f}\ln \bar{A}, \tag{60}$$

$$\tilde{t}_a = -\frac{1}{\tilde{\sigma}_f^2}[\bar{\omega}_s - \tilde{\omega}_f]. \tag{61}$$

Here it is assumed the bandwidth variations are sufficiently suppressed by windowing and filtering, so that $\tilde{\sigma}_s \approx \tilde{\sigma}_f$, and that the quadratic terms in both the amplitude and phase deviations are negligible over this bandwidth.

To set up the general expressions for these parameters, we represent the synthetic and observed cross-correlagrams in terms of the component cross-correlagrams

$$\tilde{C}_{mn}(t) = [\alpha_m(t) * \tilde{u}_m(t)] \otimes \tilde{u}_n(t), \tag{62a}$$

$$C_{mn}(t) = [\alpha_m(t) * \tilde{u}_m(t)] \otimes u_n(t). \tag{62b}$$

Equations (2) and (4) yield double summations over the component indices m and n:

$$F_i W\tilde{C}_{fs}(t) = \sum_{m=1}^{N}\sum_{n=1}^{N} F_i W\tilde{C}_{mn}(t), \tag{63a}$$

$$F_i WC_{fs}(t) = \sum_{m=1}^{N}\sum_{n=1}^{N} F_i WC_{mn}(t). \tag{63b}$$

The first expression is exact; the second is an approximation only because it includes a finite, rather than infinite, set of waveforms.

The Fourier transform of each element in the (63a) can be related to $\tilde{C}_{ff}(\omega)$ by a response operator $\tilde{D}_{mn}(\omega)$, which can be expanded in a Taylor series about $\tilde{\omega}_f$. Truncating second-order terms yields a linear form containing four

Downloaded from https://academic.oup.com/gji/article/111/2/363/753853 by guest on 25 August 2022

parameters computable directly from the reference model $\tilde{\mathbf{m}}$:

$$\bar{\tau}_q^{mn}(\bar{\omega}_f) = \bar{\tau}_q^n(\bar{\omega}_f) + \bar{\tau}_q^m(\bar{\omega}_f), \tag{64}$$

$$\bar{\tau}_p^{mn}(\bar{\omega}_f) = \bar{\tau}_p^n(\bar{\omega}_f) - \bar{\tau}_p^m(\bar{\omega}_f), \tag{65}$$

$$\bar{\tau}_a^{mn}(\bar{\omega}_f) = \bar{\tau}_a^n(\bar{\omega}_f) + \bar{\tau}_a^m(\bar{\omega}_f), \tag{66}$$

$$\bar{\tau}_g^{mn}(\bar{\omega}_f) = \bar{\tau}_g^n(\bar{\omega}_f) - \bar{\tau}_g^m(\bar{\omega}_f). \tag{67}$$

$\bar{\tau}_p^n$ and $\bar{\tau}_g^n$ are the absolute phase and group delays of the nth component waveform, each being the sum of a propagation traveltime and a set of source, receiver, and α-filter delays. Similarly, each of the amplitude parameters $\bar{\tau}_q^n$ and $\bar{\tau}_a^n$ is the sum of the delays describing the propagation attenuation and the source, receiver and α-filter amplitudes. Carrying through the same analysis as in Section 4.4, we obtain the five-parameter Gaussian-wavelet approximation,

$$F_i W\bar{C}_{mn}(t) \approx \tilde{A}_{mn}\,\mathrm{Ga}\,[\bar{\sigma}_f(t - \bar{t}_g^{mn})]\cos[\bar{\omega}_{mn}(t - \bar{t}_p^{mn})], \tag{68}$$

where $\tilde{A}_{mn} \equiv \exp(-\bar{\omega}_f \bar{t}_q^{mn})$, $\bar{\omega}_{mn} \equiv \bar{\omega}_f - \bar{\sigma}_f \bar{t}_a^{mn}$, and the $\bar{t}_x^{mn}$ are related to the $\bar{\tau}_x^{mn}$ by equations analogous to (56)–(59).

To approximate the summation (63a) as a single Gaussian wavelet, we develop its Gram–Charlier expansion and reduce it to canonical form. The six non-linear equations resulting from the latter step specify a general six-parameter Gaussian wavelet, as detailed in Appendix E. Under the assumption that the quadratic variations are negligible, the summation wavelet reduces to a five-parameter Gaussian form. One of them, the effective bandwidth $\bar{\sigma}_f$, is fixed by the autocorrelagram. Therefore, the reduction to canonical form yields a system of four implicit, non-linear equations for the unknown parameters $\{\tilde{t}_x : x = \mathrm{q, p, a, g}\}$:

$$\sum_{m,n} B_{mn}\cos\varphi_{mn} = 1, \tag{69}$$

$$\sum_{m,n} B_{mn}\sin\varphi_{mn} = 0, \tag{70}$$

$$\sum_{m,n} B_{mn}(\bar{t}_a^{mn} - \tilde{t}_a)\cos\varphi_{mn} + \sum_{m,n} B_{mn}(\bar{t}_g^{mn} - \tilde{t}_g)\sin\varphi_{mn} = 0, \tag{71}$$

$$\sum_{m,n} B_{mn}(\bar{t}_g^{mn} - \tilde{t}_g)\cos\varphi_{mn} - \sum_{m,n} B_{mn}(\bar{t}_a^{mn} - \tilde{t}_a)\sin\varphi_{mn} = 0. \tag{72}$$

Here, B_{mn} and φ_{mn} are the real-valued coefficient and phase factor defined by

$$B_{mn} = \frac{1}{\sqrt{2\pi}}\exp[-\bar{\omega}_f(\bar{t}_q^{mn} - \tilde{t}_q)]\,\mathrm{Ga}\,[\bar{\sigma}_f(\bar{t}_g^{mn} - \tilde{t}_g)], \tag{73}$$

$$\varphi_{mn} = (\bar{\omega}_f - \bar{\sigma}_f^2 \bar{t}_a^{mm})(\bar{t}_p^{mn} - \tilde{t}_p) - \bar{\sigma}_f^2(\bar{t}_a^{mn} - \tilde{t}_a)(\bar{t}_p - \tilde{t}_g). \tag{74}$$

The four time shifts $\{\tilde{t}_x : x = \mathrm{q, p, a, g}\}$ measure the interference of the extraneous waveforms after windowing and filtering. When the interference is negligible, $F_i W\bar{C}_{fs}$ equals $F_i W\bar{C}_{ff}$, and these times are all zero.

Fig. 12 plots the values of the interference time shifts for the *Sa* example. For the transverse component, all of the shifts are generally small, a few seconds or less, as expected from the isolated character of the *SH*-polarized *Sa* phase on the synthetic in Fig. 4. The sizes of the shifts are generally larger for the vertical component, owing to interference by the shear-coupled *PL* wave, which is poorly represented by the isolation filter. The largest effect is seen for $\tilde{t}_a$ at high frequencies, where it reaches −8 s. For both components, however, the interference phase delays $\tilde{t}_p$ are less than 2 s.

4.6 Perturbation formulae

In practice, we never have to solve (69)–(72), because we can determine the interference parameters by numerically fitting (8) to the synthetic cross-correlagram. It is by perturbing this system of non-linear equations, however, that we derive the theoretical relationships between the observables, $\delta t_x = t_x - \tilde{t}_x$, which are our GSDFs, and the differential dispersion parameters of the individual mode branches, $\delta\tau_x^n = \tau_x^n - \bar{\tau}_x^n$. The Fréchet kernels for the former can then be computed, since the kernels for the latter are known.

The notation needed for the perturbation expansions can be simplified by defining a set of $N \times N$ dimensionless matrices. Let $\mathbf{C}$ and $\mathbf{S}$ be the matrices with components

$$(\mathbf{C})_{mn} = B_{mn}\cos\varphi_{mn}, \tag{75}$$

$$(\mathbf{S})_{mn} = B_{mn}\sin\varphi_{mn}, \tag{76}$$

and, for x equal to either a or g, let $\mathbf{C}_x$ and $\mathbf{S}_x$ be the matrices

$$(\mathbf{C}_x)_{mn} = B_{mn}\bar{\omega}_f(\bar{t}_x^{mn} - \tilde{t}_x)\cos\varphi_{mn}, \tag{77}$$

$$(\mathbf{S}_x)_{mn} = B_{mn}\bar{\omega}_f(\bar{t}_x^{mn} - \tilde{t}_x)\sin\varphi_{mn}. \tag{78}$$

We note that in the special case when $\tilde{t}_q = \tilde{t}_p = \tilde{t}_a = \tilde{t}_g = 0$ (no interference), then $B_{mn} = B_{nm}$ and $\varphi_{mn} = -\varphi_{nm}$. These symmetries and those associated with (65) and (67) imply that, in this special case, $\mathbf{C}$, $\mathbf{C}_a$, and $\mathbf{S}_g$ are symmetric and $\mathbf{S}$, $\mathbf{S}_a$, and $\mathbf{C}_g$ are antisymmetric. Using this notation, we can write the unperturbed system (69)–(72) in the following form:

$$\mathbf{1}\cdot\mathbf{C}\cdot\mathbf{1} = 1, \tag{79}$$

$$\mathbf{1}\cdot\mathbf{S}\cdot\mathbf{1} = 0, \tag{80}$$

$$\mathbf{1}\cdot(\mathbf{C}_a + \mathbf{S}_g)\cdot\mathbf{1} = 0, \tag{81}$$

$$\mathbf{1}\cdot(\mathbf{C}_g - \mathbf{S}_a)\cdot\mathbf{1} = 0, \tag{82}$$

where $\mathbf{1}$ is the N-vector with unit components.

Variations in the component parameters, $\tilde{t}_x^n \to \tilde{t}_x^n + \delta t_x^n$, will perturb the parameters of the composite correlagram, $\tilde{t}_x \to \tilde{t}_x + \delta t_x$. We let $\delta\mathbf{t}_x$ be the N-vector whose nth component is δt_x^n, and, for the moment, proceed formally under the assumption that the perturbations are small in the sense that

$$\bar{\omega}_f\,\delta t_q^n = O(\varepsilon), \qquad \bar{\omega}_f\,\delta t_p^n = O(\varepsilon),$$
$$\bar{\sigma}_f\,\delta t_a^n = O(\varepsilon), \qquad \bar{\sigma}_f\,\delta t_g^n = O(\varepsilon), \tag{83}$$

for all n, where $\varepsilon \ll 1$ is the perturbation scaling parameter. Retaining terms to first order in ε, we obtain four linear equations,

$$\delta t_q = \mathbf{1}\cdot\mathbf{C}\cdot\delta\mathbf{t}_q + \mathbf{1}\cdot\mathbf{S}\cdot\delta\mathbf{t}_p, \tag{84}$$

$$\delta t_p = -\mathbf{1}\cdot\mathbf{S}\cdot\delta\mathbf{t}_q + \mathbf{1}\cdot\mathbf{C}\cdot\delta\mathbf{t}_p, \tag{85}$$

$$\delta t_a = -\mathbf{1}\cdot(\mathbf{C}_a + \mathbf{S}_g)\cdot\delta\mathbf{t}_q + \mathbf{1}\cdot(\mathbf{C}_g - \mathbf{S}_a)\cdot\delta\mathbf{t}_p + \mathbf{1}\cdot\mathbf{C}\cdot\delta\mathbf{t}_a + \mathbf{1}\cdot\mathbf{S}\cdot\delta\mathbf{t}_g, \tag{86}$$

$$\delta t_g = -\mathbf{1}\cdot(\mathbf{C}_g - \mathbf{S}_a)\cdot\delta\mathbf{t}_q - \mathbf{1}\cdot(\mathbf{C}_a + \mathbf{S}_g)\cdot\delta\mathbf{t}_p - \mathbf{1}\cdot\mathbf{S}\cdot\delta\mathbf{t}_a + \mathbf{1}\cdot\mathbf{C}\cdot\delta\mathbf{t}_g. \tag{87}$$

Downloaded from https://academic.oup.com/gji/article/111/2/363/753853 by guest on 25 August 2022

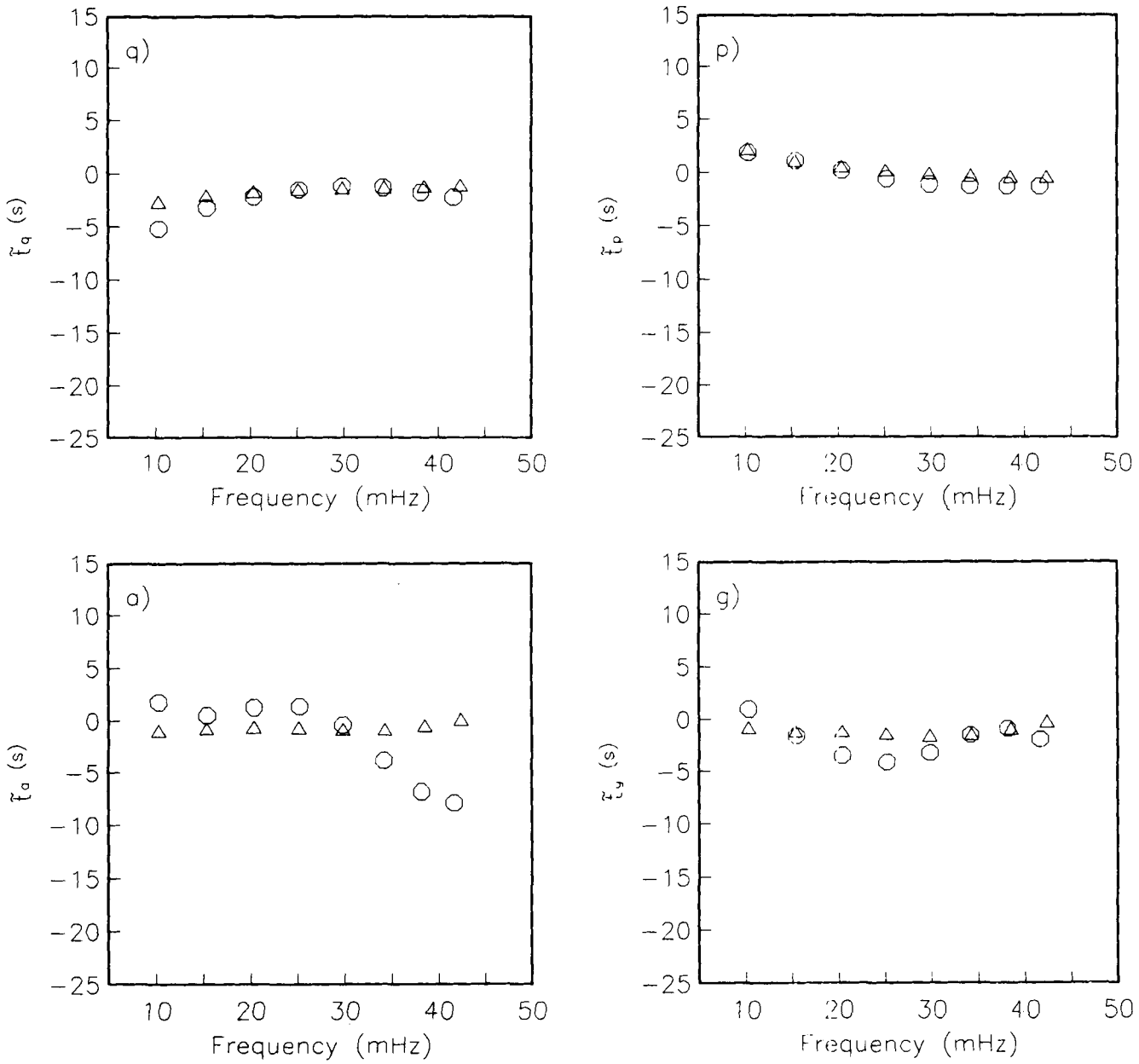

Figure 12. Interference time shifts, $\bar{t}_x$, estimated from the waveform-fitting of equation (8) to $F_i W \tilde{C}_{fs}(t)$ plotted as a function of frequency for the vertical (circles) and transverse (triangles) components.

The perturbation formulae (84)–(87) provide the requisite linearized relationships between the GSDFs and quantities computable from the individual mode branches. In particular, they show the existence of couplings among the different types of waveform parameters. The expression for the net differential phase delay δt_p, for example, depends upon averages of both the phase delays δt_p^n and amplitude differentials δt_q^n of the individual wavelets. This is physically correct. Increasing the amplitudes of the modes contributing primarily to the beginning of a wave group relative to those arriving at later times shifts the phase centre forward, even when the phases of the individual groups are not perturbed. Correspondingly, the constructive interference caused by shifting the arrival times for individual modes towards the phase centre of a wave group increases its net amplitude even when the amplitudes of the individual groups remain unaltered. Both δt_q and δt_p are stationary with respect to δt_a^n and δt_g^n. The perturbations δt_a and δt_g are not stationary with respect to δt_q^n and δt_p^n, however, and additional terms are present to account for these couplings.

The perturbation scalings given by (83) are more stringent than previously assumed to obtain the linearized equations (56)–(59) (*cf.* discussion following equation 49). Indeed, they are just as restrictive as the scalings used to linearize differential waveform perturbations. They can be relaxed, however, by noting that (84)–(87) provide *exact* solutions to the non-linear system (79)–(82) for two special cases: (1) a constant, frequency-independent amplitude perturbation, i.e., $\delta \mathbf{t_q} = t_0 \mathbf{1}$ and $\delta \mathbf{t_p} = \delta \mathbf{t_a} = \delta \mathbf{t_g} = 0$; and (2) a constant, frequency-independent traveltime perturbation, i.e.

Downloaded from https://academic.oup.com/gji/article/111/2/363/753853 by guest on 25 August 2022

$\delta\mathbf{t}_\mathbf{p} = \delta\mathbf{t}_\mathbf{g} = t_1\mathbf{1}$ and $\delta\mathbf{t}_\mathbf{q} = \delta\mathbf{t}_\mathbf{a} = 0$. The scalings can thus be revised to read

$$\bar{\omega}_\mathrm{f}(\delta t_\mathrm{q}^n - t_0) = O(\varepsilon), \qquad \bar{\omega}_\mathrm{f}(\delta t_\mathrm{p}^n - t_1) = O(\varepsilon),$$
$$\bar{\sigma}_\mathrm{f}\,\delta t_\mathrm{a}^n = O(\varepsilon), \qquad \bar{\sigma}_\mathrm{f}(\delta t_\mathrm{g}^n - t_1) = O(\varepsilon), \tag{88}$$

where t_0 and t_1 are suitably chosen constants of arbitrary magnitude. Moreover, it is clear from the form of (73) that the component cross-correlagrams for which $|\bar{t}_\mathrm{g}^{mn} - \bar{t}_\mathrm{g}| \gg \bar{\sigma}_\mathrm{f}^{-1}$ or $(\bar{t}_\mathrm{q}^{mn} - \bar{t}_\mathrm{q}) \gg \bar{\omega}_\mathrm{f}^{-1}$ will contribute negligibly to the sum, so that the scalings in (88) need only apply across a restricted set of ns. Therefore, large shifts in traveltime and large amplitude perturbations are accommodated by the linearized theory, provided that the differential variations among the waveforms which dominate the correlagram are not too great. In most applications involving compact waveforms, including the *Sa* example used here, this requirement is well satisfied. It is considerably less restrictive than needed for linearized waveform inversion.

4.7 Fréchet kernels for the structural inverse problem

Let $g_x^n(\bar{\omega}_\mathrm{f}, r)$ be the Fréchet kernel that maps the model perturbation $\delta m(r)$ into the first-order perturbation $\delta\tau_x^n(\bar{\omega}_\mathrm{f})$:

$$\delta\tau_x^n(\bar{\omega}_\mathrm{f}) = \int_0^R g_x^n(\bar{\omega}_\mathrm{f}, r)\,\delta m(r) r^2\,dr, \qquad x = \mathrm{q, p, a, g}. \tag{89}$$

Because the phase-delay functional $\delta\tau_\mathrm{p}^n$ obeys a variational principal, its perturbation can be written as in integral over the unperturbed wave function. When the component waveforms are individual travelling modes, as in the examples discussed here, the expression for $g_\mathrm{p}^n(\bar{\omega}_\mathrm{f}, r)$ is related in a simple way to the eigenfrequency kernels given by Woodhouse & Dahlen (1978). The group-delay kernel for an individual mode branch, $g_\mathrm{g}^n(\bar{\omega}_\mathrm{f}, r)$, has a more complicated analytical form, and is more difficult to compute, because it involves the first-order perturbation to the eigenfunction; appropriate numerical algorithms have been developed by Rodi *et al.* (1975) and Gilbert (1976). In general, the kernels for the amplitude functionals, $g_\mathrm{q}^n(\bar{\omega}_\mathrm{f}, r)$ and $g_\mathrm{a}^n(\bar{\omega}_\mathrm{f}, r)$, also depend on the eigenfunction perturbation. If the amplitude differences are dominated by anelasticity variations, however, equations (47) and (48) yield $\delta\tau_\mathrm{q}^n \approx \delta\tau_\mathrm{a}^n \approx \frac{1}{2}\bar{\tau}_\mathrm{p}^n\,\delta Q_n^{-1}$, where δQ_n^{-1} is the perturbation to the attenuation factor for the $(n-1)$th branch. The kernels for both of the amplitude parameters are then simply related to $g_\mathrm{p}^n(\bar{\omega}_\mathrm{f}, r)$.

Let $\delta\tau_\mathbf{x}$ be the N-vector whose components are the perburbations $\delta\tau_x^n(\bar{\omega}_\mathrm{f})$, and let $\mathbf{G}_\mathbf{x}$ be the operator whose nth row is $g_x^n(\bar{\omega}_\mathrm{f}, r)$, so that $\delta\tau_\mathbf{x} = \mathbf{G}_\mathbf{x}\cdot\delta\mathbf{m}$. In terms of the component waveforms, (57) can be written

$$\delta\mathbf{t}_\mathbf{p} = \delta\tau_\mathbf{p} + a(t_\mathrm{c}\mathbf{1} - \delta\tau_\mathbf{g}), \tag{90}$$

where $a \equiv (1 - \xi_1^2)(\bar{\omega}_\mathrm{f} - \bar{\omega}_\mathrm{c})/\bar{\omega}_\mathrm{f}$. Substituting this and the corresponding equation for $\delta\mathbf{t}_\mathbf{q}$ into (85) and using the identity (79) allows us to write the complete first-order perturbation equation

$$\delta t_\mathrm{p} = at_\mathrm{c} + \mathbf{1}\cdot[\mathbf{C}\cdot(\mathbf{G}_\mathbf{p} - a\mathbf{G}_\mathbf{g}) - \mathbf{S}\cdot(\mathbf{G}_\mathbf{q} - a\mathbf{G}_\mathbf{a})]\cdot\delta\mathbf{m}. \tag{91}$$

The integral kernel of the operator on the model perturbation defines the Fréchet derivative of δt_p with respect $\delta\mathbf{m}$. Similar expressions can be derived for the other three GSDFs. Because of the couplings among the variables in (56)–(59) and (84)–(87), their Fréchet derivatives also involve all four operators $\mathbf{G}_\mathbf{q}$, $\mathbf{G}_\mathbf{p}$, $\mathbf{G}_\mathbf{a}$ and $\mathbf{G}_\mathbf{g}$. This complication makes them inconvenient for application to structural inverse problems.

For a large, useful class of isolation filters, however, the couplings among the GSDFs will be sufficiently weak that their Fréchet kernels can be greatly simplified. Figs 13 and 14 display the four vectors $\mathbf{1}\cdot\mathbf{C}$, $\mathbf{1}\cdot\mathbf{S}$, $\mathbf{1}\cdot(\mathbf{C}_\mathbf{a} + \mathbf{S}_\mathbf{g})$, and $\mathbf{1}\cdot(\mathbf{C}_\mathbf{g} - \mathbf{S}_\mathbf{a})$ computed for the two polarizations of *Sa* at 30 mHz. By (79)–(82), the components of the first sum to unity, and those of the latter three sum to zero. On the vertical component, only the mode branches 2–5, which dominate the *Sa* isolation filter at this frequency, have significant amplitudes. On the transverse component, the mode branches 23–24 also show significant amplitude, representing the interference of the core reflection ScS_2 with *Sa* on the cross-correlagram.

To the extent that the δt_x^n's for these modes are slowly varying functions of n, the oscillatory nature of the vectors $\mathbf{1}\cdot\mathbf{S}$, $\mathbf{1}\cdot(\mathbf{C}_\mathbf{a} + \mathbf{S}_\mathbf{g})$, and $\mathbf{1}\cdot(\mathbf{C}_\mathbf{g} - \mathbf{S}_\mathbf{a})$ implies that the cross-coupling terms in (84)–(87) will average nearly to zero. If this averaging is effective, the perturbation equations can be reduced to the common form,

$$\delta t_x \approx \mathbf{1}\cdot\mathbf{C}\cdot\delta\mathbf{t}_\mathbf{x} = \sum_{m,n} B_{mn}\cos\varphi_{mn}\,\delta t_x^n, \quad x = \mathrm{q, p, a, g}. \tag{92}$$

We note that (92) is an especially good approximation for δt_q and δt_p, since the only cross-couplings in (84) and (85) involve contractions over $\mathbf{1}\cdot\mathbf{S}$, whose components are relatively small for all n. This results from the fact that the matrix $\mathbf{S}$ is approximately symmetric about its anti-diagonal, as well as anti-symmetric about its diagonal.

When (92) applies, the linearized relationships between the δt_x's and the $\delta\tau_x$'s allow us to express (89) in the simplified form

$$\delta\tau_x = \int_0^R g_x(\bar{\omega}_\mathrm{f}, r)\,\delta m(r) r^2\,dr \approx \mathbf{1}\cdot\mathbf{C}\cdot\mathbf{G}_\mathbf{x}\cdot\delta\mathbf{m}. \tag{93}$$

In other words, the measured differential time δt_p can first be corrected for windowing and filtering effects by solving (56)–(59) to obtain $\delta\tau_\mathrm{p}$, and this corrected phase delay can then be inverted using (93). Under approximation (92), the Fréchet derivatives of the $\delta\tau_x$'s with respect to $\delta\mathbf{m}$ are all operators of the form $\mathbf{g}_\mathbf{x} = \mathbf{1}\cdot\mathbf{C}\cdot\mathbf{G}_\mathbf{x}$; i.e., their Fréchet kernels are

$$g_x(\bar{\omega}_\mathrm{f}, r) = \sum_{n=1}^{N} c_n\,g_x^n(\bar{\omega}_\mathrm{f}, r), \tag{94}$$

where the coefficient c_n is the nth component of the vector $\mathbf{1}\cdot\mathbf{C}$,

$$c_n = \sum_{m=1}^{N} B_{mn}\cos\varphi_{mn}. \tag{95}$$

The phase-delay kernels displayed in Fig. 7 were calculated from these expressions using the coefficients displayed in Figs 15 and 16. Evident in these plots are an increase in the dominant mode number of the *Sa* isolation filter with frequency and, at the higher frequencies on the transverse component, the influence of ScS_2 interference.

Downloaded from https://academic.oup.com/gji/article/111/2/363/753853 by guest on 25 August 2022

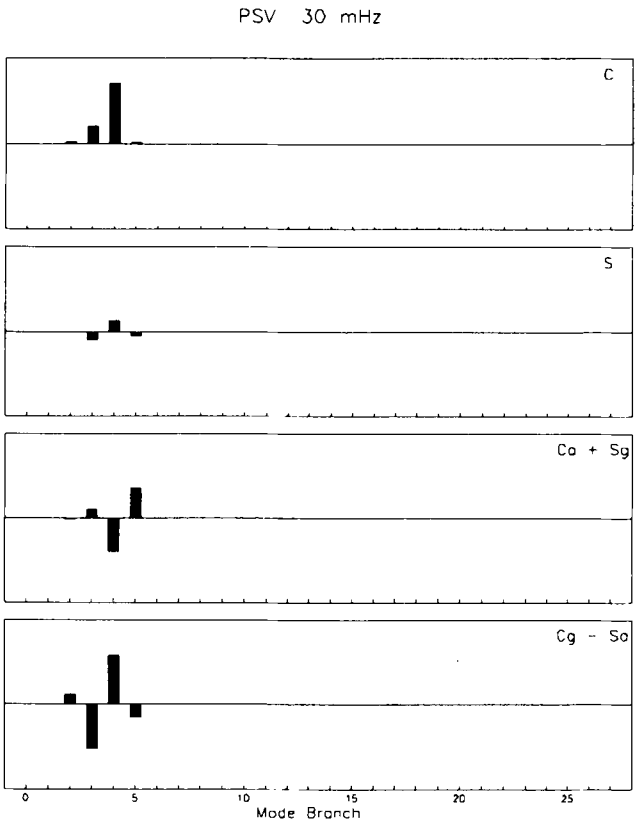

Figure 13. The four vectors $\mathbf{1}\cdot\mathbf{C}$, $\mathbf{1}\cdot\mathbf{S}$, $\mathbf{1}\cdot(\mathbf{C}_a+\mathbf{S}_g)$, and $\mathbf{1}\cdot(\mathbf{C}_g-\mathbf{S}_a)$ computed for the vertical (P–SV) component polarization of *Sa* at 30 mHz as a function of travelling-wave branch.

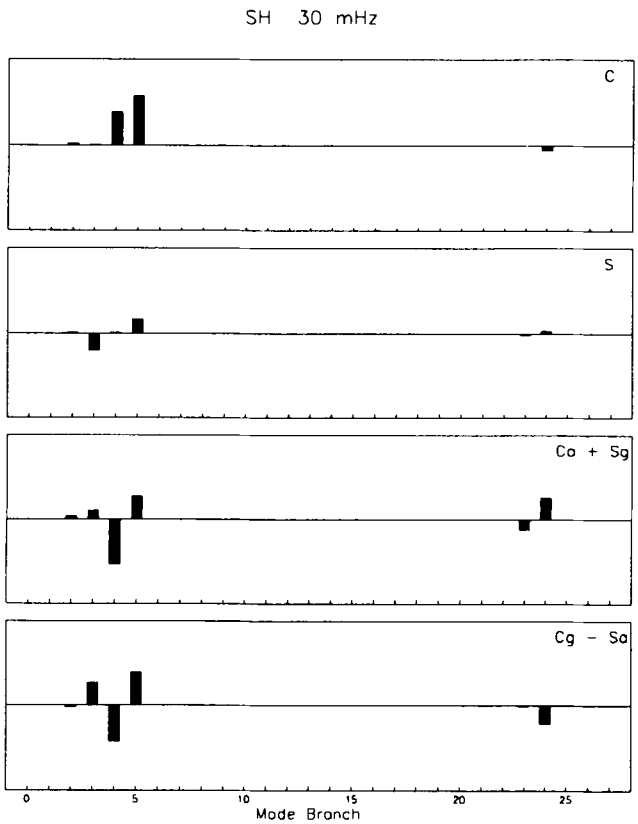

Figure 14. The four vectors $\mathbf{1}\cdot\mathbf{C}, \mathbf{1}\cdot\mathbf{S}, \mathbf{1}\cdot(\mathbf{C}_a+\mathbf{S}_g)$, and $\mathbf{1}\cdot(\mathbf{C}_g-\mathbf{S}_a)$ computed for the transverse (SH) component polarization of *Sa* at 30 mHz as a function of travelling-wave branch.

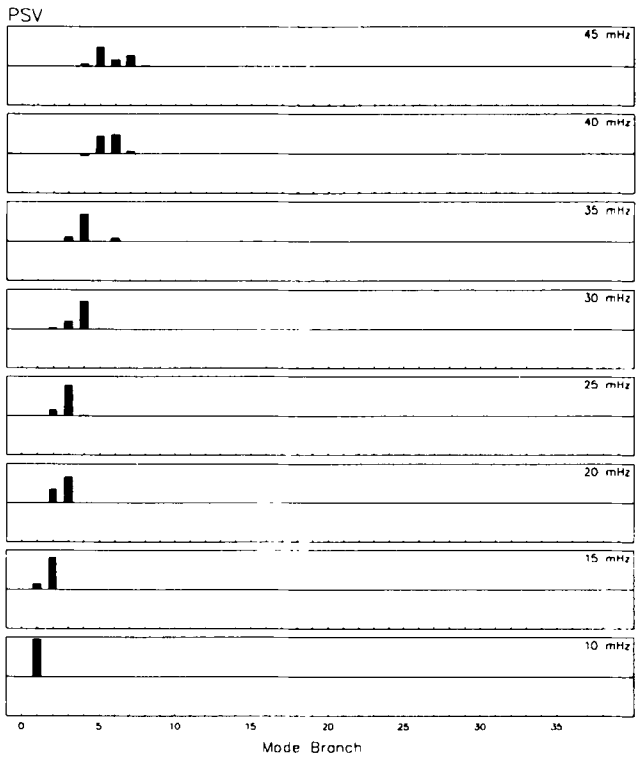

Figure 15. The phase-delay kernel coefficients c_n computed for the vertical (P–SV) component polarization of *Sa* as a function of branch number corresponding to the kernels displayed in Fig. 7.

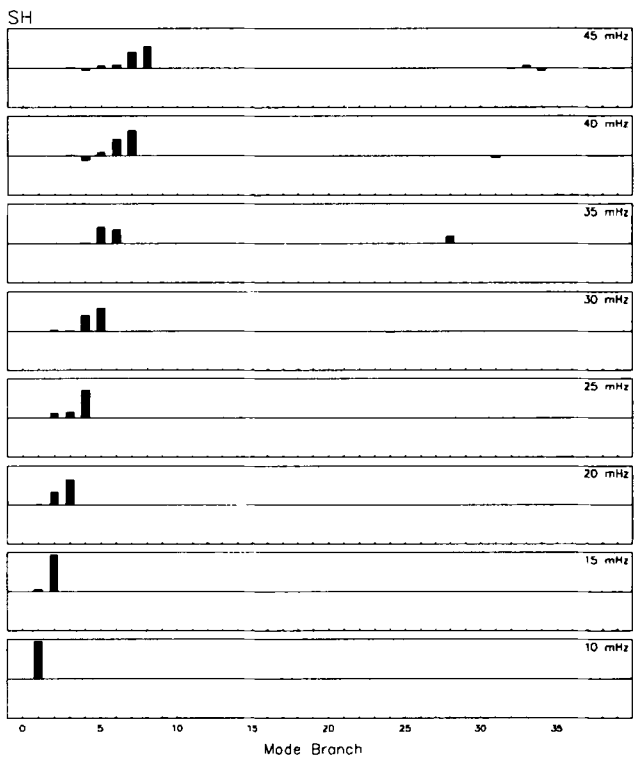

Figure 16. The phase-delay kernel coefficients c_n computed for the transverse (SH) component polarization of *Sa* as a function of branch number corresponding to the kernels displayed in Fig. 7.

Downloaded from https://academic.oup.com/gji/article/111/2/363/753853 by guest on 25 August 2022

DISCUSSION AND CONCLUSIONS

In this paper we have developed a theory for extracting phase and amplitude information from complex waveforms recorded on broad-band seismograms and for interpreting this information in terms of earth structure. The basic tool is the isolation filter (4), a composite waveform constructed for a reference earth model to select data from a desirable portion of the seismogram. When the cross-correlation between this synthetic waveform and an observed seismogram is localized in the time domain by windowing and in the frequency domain by narrow-band filtering, the resulting cross-correlagram can be approximated by a five-parameter Gaussian wavelet (5). One of these five parameters is the bandwidth of the correlagram, specified by the narrow-band filter; the other four define a set of time-like, frequency-dependent quantities $\{\delta t_x : x = \mathrm{q, p, a, g}\}$, which are functionals of earth structure. δt_p is the differential phase delay and δt_g is the differential group delay of the observed waveform relative to the synthetic, and δt_q and δt_a are the corresponding frequency-dependent amplitude parameters. For body waves whose amplitudes are controlled primarily by dissipation due to internal friction, the latter correspond to differential versions of the conventional t^* parameter. We have developed a procedure for measuring the four generalized seismological data functionals by fitting a Gaussian wavelet to the windowed, filtered cross-correlagram (equations 9–12).

To relate the GSDFs to earth structure, we apply corrections to the differential times for the effects of windowing and filtering. Solving a linear system of four equations in four unknowns (equations 56–59) yields a set of differential dispersion parameters $\{\delta\tau_x : x = \mathrm{q, p, a, g}\}$. Formulae expressing the perturbations of the GSDFs in terms of the perturbations to the dispersion parameters for the individual component waveforms, including all interference effects, have been derived (equations 84–87). Under a set of approximations valid for a large class of isolation filters, these can be simplified to yield easily computed expressions for the Fréchet kernels of the $\delta\tau_x$'s (equation 93). The calculation of these Fréchet kernels requires no high-frequency approximations.

The power of the theory resides in its generality. To illustrate the specifics of the methodology, we have here employed the travelling modes of a SNREI earth model to construct the isolation filters and Fréchet kernels for an *Sa* waveform; the basic theory can just as well be applied to other types of wavefield representations, however. In some applications, for example, it may be more efficient to take the component waveforms in (1) to be generalized ray contributions. It may also be advantageous to compute the waveforms and Fréchet kernels using a two- or three-dimensional reference model, rather than relying on a one-dimensional, path-average approximation. In the context of a modal representation, first-order scattering theory (Woodhouse 1983; Tromp & Dahlen 1990; Li & Tanimoto 1992) is easily adapted for this purpose.

We are applying the GSDF methodology to various observational problems, including upper mantle anisotropy (Gaherty *et al.* 1992) and core diffraction (Gee & Jordan 1990). We have also begun to investigate isolation filters constructed to optimize the sampling of a particular feature in the Earth's interior, rather than relying on the standard taxonomy of seismological phases. An approach of this sort may be especially fruitful for the study of deep-seated features, such as the shear velocity structure of the inner core.

ACKNOWLEDGMENTS

We thank Guust Nolet for a helpful review. This work was sponsored by the National Science Foundation under Grant EAR-8904710 and by the Air Force through the Air Force Graduate Fellowship programme.

REFERENCES

Backus, G. E., 1962. Long-wave elastic anisotropy produced by horizontal layering, *J. geophys. Res.*, **67,** 4427–4440.

Backus, G. E. & Gilbert, J. F., 1967. Numerical applications of a formalism for geophysical inverse problems, *Geophys. J. R. astr. Soc.*, **13,** 247–276.

Båth, M. & Lopez-Arroyo, A., 1963. *Pa* and *Sa* waves and the upper mantle, *Geofis pura appl.*, **56,** 67–92.

Brune, J. N., 1964. Traveltimes, body waves, and normal modes of the Earth, *Bull seism. Soc. Am.*, **54,** 2099–2128.

Burdick, L. J., 1978. t^* for *S* waves with a continental ray path, *Bull. seism. Soc. Am.*, **68,** 1013–1030.

Caloi, P., 1953. Onde longitudinali e trasversali guidate dall'astenosfera, *Rend. Sc. fis. mat. e nat.*, **XV,** 352–357.

Capon, J., 1969. High-resolution frequency–wavenumber spectrum analysis, *Proc. IEEE*, **57,** 1408–1418.

Cara, M., 1976. Observations d'ondes *Sa* de type *SH*, *Pageoph*, **114,** 141–157.

Cara, M., 1979. Lateral variations of *S* velocity in the upper mantle from higher Rayleigh modes, *Geophys. J. R. astr. Soc.*, **57,** 649–670.

Cara, M. & Lévêque, J. J., 1987. Waveform inversion using secondary observables, *Geophys. Res. Lett.*, **14,** 1046–1049.

Dziewonski, A. M. & Anderson, D. L., 1981. Preliminary reference Earth model, *Phys. Earth planet. Inter.*, **25,** 297–356.

Dziewonski, A. M. & Steim, J. M., 1982. Dispersion and attenuation of mantle waves through waveform inversion, *Geophys. J. R. astr. Soc.*, **70,** 503–527.

Dziewonski, A. M. & Woodhouse, J. H., 1987. Global Images of the Earth's interior, *Science*, **236,** 37–48.

Dziewonski, A. M., Mills, J. & Bloch, S., 1972. Residual dispersion measurement—a new method of surface-wave analysis, *Bull. seism. Soc. Am.*, **62,** 129–139.

Dziewonski, A. M., Franzen, J. E. & Woodhouse, J. H., 1984. Centroid-moment tensor solutions for January–March, 1984, *Phys. Earth planet, Inter.*, **34,** 209–219.

Gaherty, J. B., Jordan, T. H. & Gee, L. S., 1992. Radial anisotropy of oceanic and continental upper mantle: joint inversion of surface-wave, turning-ray, and *ScS*-reverberation data (abstract), *Seism. Res. Lett.*, **63,** 63.

Gee, L. S. & Jordan, T. H., 1988. Polarization anisotropy and fine-scale structure of the Eurasian upper mantle, *Geophys. Res. Lett.*, **15,** 824–827.

Gee, L. S. & Jordan, T. H., 1990. Structure at the core–mantle boundary from frequency-dependent traveltimes (abstract), *EOS*, **71,** 1289.

Gee, L. S., Lerner-Lam, A. L. & Jordan, T. H., 1985. Resolving power of higher-mode waveform inversion for Eurasian upper-mantle structure, *AFGL-TR*-85-0206, 1–36.

Gilbert, J. F., 1976. Differential kernels for group velocity, *Geophys. J. R. astr. Soc.*, **44,** 649–660.

Herrin, E. & Goforth, T., 1977. Phase-matched filters: application

Downloaded from https://academic.oup.com/gji/article/111/2/363/753853 by guest on 25 August 2022

to the study of Rayleigh waves, *Bull. seism. Soc. Am.*, **67,** 1259–1275.

Hille, E., 1926. A class of reciprocal functions, *Ann. math.*, **27,** 427–464.

Jackson, D., 1961. *Fourier Series and Orthogonal Polynomials,* Carus Mathematical Monographs, no. 6, 5th ed., Mathematical Association of American, Monash, WI, 234pp.

Jordan, T. H., 1980. Earth structure from seismological observations, in Physics of the Earth's Interior, *Proc. Int. School Phys. Enrico Fermi, 77*, pp. 1–40, eds Dziewonski, A. M. & Boschi, E., Soc. Italiana de Fisisca, Bologna.

Jordan, T. H., Lerner-Lam, A. L. & Creager, K. C., 1989. Seismic imaging of boundary layers and deep mantle convection, in *Mantle Convection: Plate Tectonics and Global Dynamics*, pp. 97–210, ed. Peltier, W. R., Gordon and Breach, NY.

Julian, B. R., Davies, D. & Sheppard, R. M., 1972. *PKJKP, Nature,* **235,** 317–318.

Lebedev, N. N., 1965. *Special Functions and their Applications*, ed. Silverman, R., Prentice-Hall, Englewood Cliffs, NJ, 308pp.

Lerner-Lam, A. L. & Jordan, T. H., 1983. Earth structure from fundamental and higher-mode waveform analysis, *Geophys. J. R. astr. Soc.*, **75,** 759–797.

Lerner-Lam, A. L. & Jordan, T. H., 1987. How thick are the continents? *J. geophys. Res.*, **92,** 14 007–14 026.

Li, X-D. & Tanimoto, T., 1992. Waveforms of long-period body waves in a slightly aspherical Earth model, *Geophys. J. Int.*, in press.

Luo, Y. & Schuster, G. T., 1991a. Wave equation inversion of skeletalized geophysical data, *Geophys. J. Int.*, **105,** 289–294.

Luo, Y. & Schuster, G. T., 1991b. Wave equation traveltime inversion, *Geophysics,* **56,** 645–653.

Mellman, G. R., 1980. A method of bodywave waveform inversion for the determination of earth structure, *Geophys. J. R. astr. Soc.*, **62,** 481–504.

Nolet, G., 1977. The upper mantle structure under western Europe inferred from the dispersion of Rayleigh modes, *J. Geophys.*, **43,** 265–285.

Nolet, G., 1990. Partitioned waveform inversion and 2-D structure under the NARS array, *J. geophys. Res.*, **95,** 8499–8512.

Palamà, G., 1937. Sui polinomi di Legendre di Laguerre e di Hermite, *Reale Istituto Lombardo di Scienze e Lettere, Rendiconti,* **LXX,** 147–191.

Rietz, H. L., 1971. *Mathematical Statistics,* Carus Mathematical Monographs, no. 3, 6th ed., Mathematical Association of America, La Salle, IL, 181pp.

Rodi, W. L., Glover, P., Li, T. M. C. & Alexander, S. S., 1975. A fast, accurate method for computing group-velocity partial derivatives for Rayleigh and Love modes, *Bull. seism. Soc. Am.*, **65,** 1105–1114.

Rothman, D. H., 1985. Nonlinear inversion, statistical mechanics, and residual statics estimation, *Geophysics,* **50,** 2784–2796.

Sansone, G. 1959. *Orthogonal Functions,* Pure and Applied Mathematics, vol. IX, Intersciences Publishers, New York, 411pp.

Scales, J. A., Smith, M. L. & Fischer, T. L., 1991. Statistical methods of global optimization and their application to seismic inverse theory, preprint.

Scales, J. A., Smith, M. L. & Fischer, T. L., 1992. Global optimization methods for multimodal inverse problems, *J. Comp. Phys.*, in press.

Schwab, F., Kausel, E. G. & Knopoff, L., 1974. Interpretation of *Sa* for a shield structure, *Geophys. J. R. astr. Soc.*, **36,** 737–742.

Sipkin, S. A. & Jordan, T. H., 1980. Multiple *ScS* traveltimes in the western Pacific: implications for mantle heterogeneity, *J. geophys. Res.*, **85,** 853–861.

Szegö, G., 1926. Beiträge zur theorie der Laguerreschen polynome. I.: Entwicklungssätze, *Math. Zeitschrift,* **25,** 87–115.

Tanimoto, T., 1984. Waveform inversion of mantle Love waves: the Born seismogram approximation, *Geophys. J. R. astr. Soc.*, **78,** 641–660.

Tanimoto, T., 1987. The 3-D shear wave structure in the mantle by overtone waveform inversions—II. Inversion of *X*-waves, *R*-waves, and *G*-waves, *Geophys. J. R. astr. Soc.*, **93,** 321–334.

Tarantola, A., 1986. A strategy for nonlinear elastic inversion of siesmic reflection data, *Geophysics,* **51,** 1893–1903.

Tromp, J. & Dahlen, F. A., 1990. Summation of the Born series for the normal modes of the Earth, *Geophys. J. Int.*, **100,** 527–533.

Vinnik, L. P., 1977. Detection of waves converted from *P* to *SV* in the mantle, *Phys. Earth planet. Inter.*, **15,** 39–45.

Woodhouse, J. H., 1983. The joint inversion of seismic waveforms for lateral variations in earth structure and earthquake source parameters, in *Earthquakes: Observation, Theory and Interpretation, Proc. Int. School Phys. Enrico Fermi,* 85, pp. 366–397, eds Kanamori, H. & Boschi, E., Soc. Italiana de Fisisca, Bologna.

Woodhouse, J. H. & Dahlen, F. A., 1978. The effect of a general aspherical perturbation on the free oscillations of the Earth, *Geophys. J. R. astr. Soc.*, **53,** 335–354.

Woodhouse, J. H. & Dziewonski, A. M., 1984. Mapping the upper mantle: three-dimensional modeling of the earth structure by inversion of seismic waveforms, *J. geophys. Res.*, **89,** 5953–5986.

APPENDIX A: GAUSSIAN WAVELETS

A Gaussian wavelet is a function of the form $g(t) = \mathcal{R}e[e^{i\phi(t)}]$ where ϕ is a complex-valued, quadratic polynomial in time t. Six real numbers are needed to specify the polynomial; hence, we call this general function a *six-parameter Gaussian wavelet.* Any such wavelet can be expressed as the product of a Gaussian envelope with amplitude A and half-width $\alpha^{-1/2}$ centred at a time t_0, and the cosine of a quadratic phase function with a value ϕ_0, slope ω_0, and curvature β at t_0:

$$g(t) = A \exp[-\tfrac{1}{2}\alpha(t-t_0)^2] \cos[\phi_0 + \omega_0(t-t_0) + \tfrac{1}{2}\beta(t-t_0)^2]. \quad \text{(A1)}$$

To ensure that $g(t) \to 0$ as $|t| \to \infty$, we require α to be strictly positive. Without loss of generality, we may also choose A and ω_0 to be positive. We note that ω_0 is the instantaneous frequency of $g(t)$ at t_0. Defining the quantities

$$\nu^2 = \alpha + i\beta, \quad \text{(A2)}$$

$$t_1 = t_0 - \phi_0/\omega_0, \quad \text{(A3)}$$

allows us to write

$$g(t) = A\, \mathcal{R}e\left\{\exp\left[-\frac{\nu^2}{2}(t-t_0)^2 - i\omega_0(t-t_1)\right]\right\}. \quad \text{(A4)}$$

If $\alpha < \omega_0^2$, then, in the vicinity of ω_0, the contribution of the spectral peak at $-\omega_0$ can be neglected, and the Fourier transform

Downloaded from https://academic.oup.com/gji/article/111/2/363/753853 by guest on 25 August 2022

of (A4) is given by

$$g(\omega) = A\frac{\sqrt{2\pi}}{\nu}\,\mathrm{Ga}\left[\frac{\omega-\omega_0}{\nu}\right]e^{i[\omega_0 t_1+(\omega-\omega_0)t_0]}, \tag{A5}$$

which can be recast in the form

$$g(\omega) = A\frac{\sqrt{2\pi}}{\nu}\,\mathrm{Ga}\left[\frac{\omega-\omega_0}{\sigma_0}\right]e^{i[\omega_0 t_1+(\omega-\omega_0)t_0+\frac{1}{2}\gamma(\omega-\omega_0)^2]}, \tag{A6}$$

where $\mathrm{Ga}(z) \equiv e^{-z^2/2}$, and the half-bandwidth σ_0 and phase curvature γ are real numbers related to the other parameters by

$$\nu^{-2} = \sigma_0^{-2} - i\gamma, \tag{A7}$$

$$\sigma_0^2 = \alpha(1+\beta^2/\alpha^2) > 0, \tag{A8}$$

$$\gamma = 1/[\beta(1+\alpha^2/\beta^2)]. \tag{A9}$$

The special case when phase function is linear, i.e. when $\beta = \gamma = 0$, defines a *five-parameter Gaussian wavelet.* Then, $\nu = \alpha^{1/2} = \sigma_0$ is the half-bandwidth of the spectrum, t_0 is the group delay, t_1 is the phase delay, and the time-domain expression reduces to the same form as equation (5);

$$g(t) = A\,\mathrm{Ga}\,[\sigma_0(t-t_0)]\cos[\omega_0(t-t_1)]. \tag{A10}$$

In a five-parameter wavelet, σ_0 is constrained to be real; in a six-parameter wavelet, it is allowed to be complex. The former describes narrow-band waveforms with approximately linear dispersion functions, while the latter is needed for the analysis of quadratic dispersion (see Appendix D).

APPENDIX B: HERMITE POLYNOMIALS

The properties of the Hermite polynomials, defined in the text by (16), are discussed by Hille (1926), Szegö (1926), Palamà (1937), Sansone (1959) and Lebedev (1965). Hermite polynomials form a complete set over the interval $(-\infty, \infty)$ and are orthogonal with respect to a Gaussian weight:

$$\int_{-\infty}^{\infty} \mathrm{Ga}\,(x)\,\mathrm{He}_k(x)\,\mathrm{He}_m(x)\,dx = \sqrt{2\pi}\,k!\,\delta_{km}. \tag{B1}$$

The first seven Hermite polynomials are plotted in Fig. B1:

$$\begin{aligned} &\mathrm{He}_0(x) = 1, && \mathrm{He}_1(x) = x,\\ &\mathrm{He}_2(x) = x^2 - 1, && \mathrm{He}_3(x) = x^3 - 3x,\\ &\mathrm{He}_4(x) = x^4 - 6x^2 + 3, && \mathrm{He}_5(x) = x^5 - 10x^3 + 15x,\\ &\mathrm{He}_6(x) = x^6 - 15x^4 + 45x^2 - 15. \end{aligned} \tag{B2a–g}$$

The $\mathrm{He}_k(x)$ are related to an alternative set of Hermite polynomials, usually denoted $\mathrm{H}_k(x)$, through a simple scaling: $\mathrm{He}_k(x) = 2^{-k/2}\mathrm{H}_k(x/\sqrt{2})$. The latter are more commonly employed in mathematical physics, while the former are more prevalent in probability and statistics.

The Hermite polynomials have the following properties with respect to negation, shifting and scaling of their argument:

$$\mathrm{He}_k(-x) = (-1)^k\,\mathrm{He}_k(x), \tag{B3}$$

$$\mathrm{He}_k(x-x_0) = \sum_{m=0}^{k} \frac{k!}{m!\,(k-m)!}(x_1-x_0)^m\,\mathrm{He}_{k-m}(x-x_1), \tag{B4}$$

$$\mathrm{He}_k\left(\frac{x}{x_0}\right) = \left(\frac{x_1}{x_0}\right)^k \sum_{m=0}^{(k/2)} \frac{k!\,(1/2)^m}{m!\,(k-2m)!}\left(1-\frac{x_0}{x_1}\right)^m \mathrm{He}_{k-2m}\left(\frac{x}{x_1}\right). \tag{B5}$$

These expressions can be used to obtain general formulae relating shifted and scaled sums of Hermite polynomials:

$$\sum_{k=0}^{\infty} a_k\,\mathrm{He}_k(x-x_0) = \sum_{m=0}^{\infty} b_m\,\mathrm{He}_m(x-x_1); \qquad b_m = \sum_{k=0}^{\infty} \frac{(k+m)!}{m!\,k!}(x_1-x_0)^k a_{k+m}, \tag{B6}$$

$$\sum_{k=0}^{\infty} c_k\,\mathrm{He}_k\left(\frac{x}{x_0}\right) = \sum_{m=0}^{\infty} d_m\,\mathrm{He}_m\left(\frac{x}{x_1}\right); \qquad d_m = \left(\frac{x_1}{x_0}\right)^m \sum_{k=0}^{\infty} \frac{(2k+m)!\,(-1/2)^k}{m!\,k!}\left(1-\frac{x_1^2}{x_0^2}\right)^k c_{2k+m}. \tag{B7}$$

Downloaded from https://academic.oup.com/gji/article/111/2/363/753853 by guest on 25 August 2022

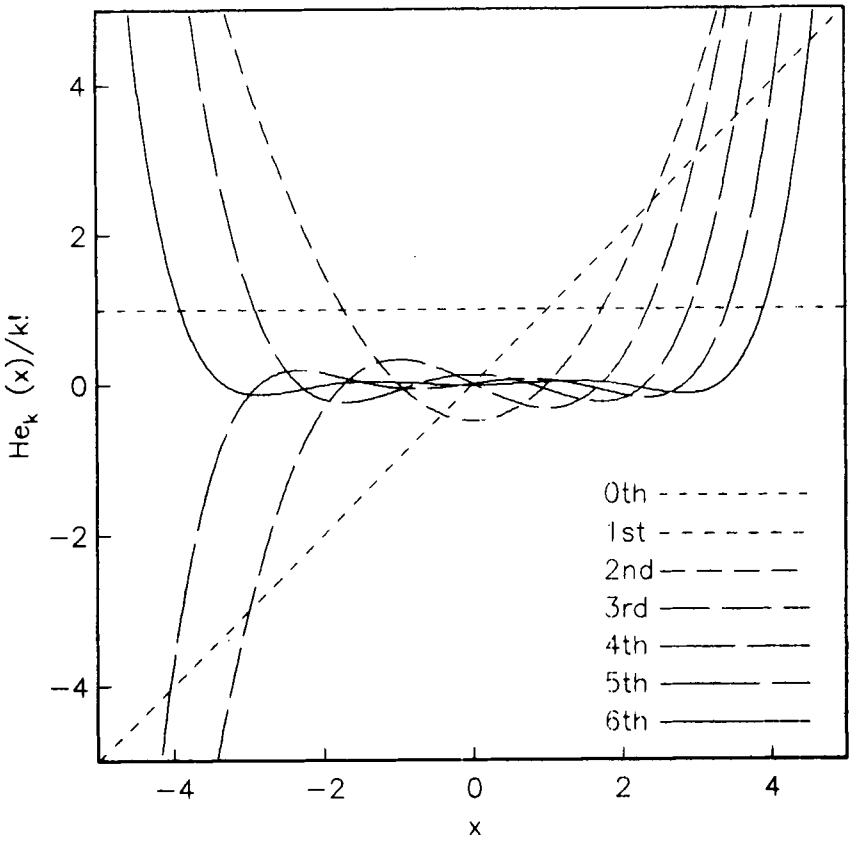

Figure B1. A plot of the scaled Hermite polynomials $He_k(x)/k!$ for degrees 0 to 6.

The Fourier-transform properties of Hermite polynomials are given by the transform pair:

$$\int_{-\infty}^{\infty} A\, e^{-i\omega_0(t-t_1)}\, Ga\,[v(t-t_0)][-iv(t-t_0)]^k\, e^{i\omega t}\, dt = \frac{\sqrt{2\pi}}{v} A e^{i[\omega_0 t_1 + (\omega-\omega_0)t_0]}\, Ga\left(\frac{\omega-\omega_0}{v}\right) He_k\left(\frac{\omega-\omega_0}{v}\right), \tag{B8}$$

$$\frac{1}{2\pi}\int_{-\infty}^{\infty} \frac{\sqrt{2\pi}}{v} A e^{i[\omega_0 t_1 + (\omega-\omega_0)t_0]}\, Ga\left(\frac{\omega-\omega_0}{v}\right) He_k\left(\frac{\omega-\omega_0}{v}\right) e^{-i\omega t}\, d\omega = A e^{-i\omega_0(t-t_1)}\, Ga\,[v(t-t_0)][-iv(t-t_0)]^k. \tag{B9}$$

In these formulae and elsewhere, $Ga\,(z) \equiv e^{-z^2/2}$.

APPENDIX C: GRAM–CHARLIER SERIES

In seismology, the two basic operations applied to correlagrams are time-domain localization by windowing and frequency-domain localization by narrow-band filtering. Here we develop the calculus for expressing these operations analytically in terms of Gram–Charlier series.

Canonical representation of real functions

The spectrum of an arbitrary function $C(\omega)$ can be expanded in Hermite polynomials $\{He_k(\omega): k = 0, 1, 2, \ldots\}$. When pre-multiplied by a Gaussian function, $Ga\,(\omega)$, this expansion is referred to as a Gram–Charlier series (Jackson 1961; Rietz 1971). We generalize the usual form of these series by considering an expansion where the pre-multiplier is the spectrum of a general Gaussian wavelet, given in equation (A5). Because $C(t)$ is real-valued, we can limit our consideration to positive

Downloaded from https://academic.oup.com/gji/article/111/2/363/753853 by guest on 25 August 2022

frequencies. Let $\{a_k\}$ be complex coefficients such that

$$C_+(\omega) \equiv C(\omega)\mathrm{H}(\omega) = A\frac{\sqrt{2\pi}}{\nu}\mathrm{e}^{i[\omega_0 t_1 + (\omega-\omega_0)t_0]}\,\mathrm{Ga}\left(\frac{\omega-\omega_0}{\nu}\right)\sum_{k=0}^{\infty} a_k\,\mathrm{He}_k\left(\frac{\omega-\omega_0}{\nu}\right), \tag{C1}$$

where $\mathrm{H}(\omega)$ is the Heaviside step function. Then, the spectrum at negative frequencies can be recovered using its Hermitian symmmetry: $C(-\omega) = C_+^*(\omega)$.

There are six parameters in (C1): an amplitude scale A, a frequency location parameter ω_0, a complex bandwidth scale parameter ν with $\nu^{-2} \equiv \sigma_0^{-2} - i\gamma$ and two time shift parameters t_0 and t_1. The expansion coefficients a_k may be determined by rearranging (C1), multiplying both sides by $\mathrm{He}_m[(\omega-\omega_0)/\nu]$ and integrating over the interval $(-\infty, \infty)$. The orthogonality condition (B1) yields

$$a_k = \frac{1}{2\pi k!}\frac{1}{A}\int_0^{\infty} C(\omega)\mathrm{e}^{-i[\omega_0 t_1 + (\omega-\omega_0)t_0]}\,\mathrm{He}_k\left(\frac{\omega-\omega_0}{\nu}\right)d\omega, \tag{C2}$$

for the kth coefficient.

We obtain a time-domain expression for $C(t)$ by making use of the Fourier transform properties of Hermite polynomials (B9):

$$C(t) = A\,\mathscr{R}e\left\{\mathrm{e}^{-i\omega_0(t-t_1)}\,\mathrm{Ga}\,[\nu(t-t_0)]\sum_{k=0}^{\infty} a_k[-i\nu(t-t_0)]^k\right\}. \tag{C3}$$

We say that the Gram–Charlier expansion is in its canonical form when the first three coefficients satisfy the relations: $a_0 = 1$, $a_1 = a_2 = 0$. The real and imaginary parts of these equations specify a system of six equations in the six parameters of the Gram–Charlier expansion.

In the case where the phase-curvature parameter is small, $\gamma \approx 0$ and the six-parameter system reduces to five:

$$C(t) = A\,\mathscr{R}e\left\{\mathrm{e}^{-i\omega_0(t-t_1)}\,\mathrm{Ga}\,[\sigma_0(t-t_0)]\sum_{k=0}^{\infty} a_k[-i\sigma_0(t-t_0)]^k\right\}, \tag{C4}$$

which is the basis for the derivations in the text. Appendix D describes some results obtained from the six-parameter representation.

Windowing theorem

In the case of a windowing operator which is a real-valued, one-sided, even function centred at a lag-time t_w, the time-domain image of its canonical Gram–Charlier expansion can be written as a series in even powers of t:

$$W(t) = \mathrm{Ga}\,[\sigma_w(t-t_w)]\{1 + b_4[\sigma_w(t-t_w)]^4 - b_6[\sigma_w(t-t_w)]^6 + \cdots\}, \tag{C5}$$

where σ_w is the half-width of its Fourier spectrum $W(\omega)$ and the coefficients are determined by the spectral integrals of Hermite polynomials given by (23).

The windowing theorem states

$$\begin{aligned} W(t)C(t) &= \mathscr{R}e\,\{A\mathrm{e}^{-i\omega_0(t-t_1)}\,\mathrm{Ga}\,[\sigma_w(t-t_w)]\,\mathrm{Ga}\,[\nu(t-t_0)]\sum_{m=0}^{\infty} b_m[-i\sigma_w(t-t_w)]^m\sum_{k=0}^{\infty} a_k[-i\nu(t-t_0)]^k\} \\ &= \mathscr{R}e\,\{A\mathrm{e}^{-i\omega_0(t-t_1)}\,\mathrm{Ga}\left[\frac{\sigma_w\nu}{\sigma_0'}(t_w-t_0)\right]\mathrm{Ga}\,[\sigma_0'(t-t_0')]\sum_{k=0}^{\infty} c_k[-i\sigma_0'(t-t_0')]^k\Big\}, \end{aligned} \tag{C6}$$

with coefficients that are given by a convolutional sum over two infinite sums

$$c_k = \sum_{m=0}^{k}\left\{\left(\frac{\nu}{\sigma_0'}\right)^m\sum_{l=0}^{\infty}\frac{(m+l)!}{m!\,l!}[-i\nu(t_0'-t_0)]^l\,a_{l+m}\right\}\left\{\left(\frac{\sigma_w}{\sigma_0'}\right)^{k-m}\sum_{n=0}^{\infty}\frac{(k-m+n)!}{(k-m)!\,n!}[-i\sigma_w(t_0'-t_w)]^n\,b_{n+k-m}\right\}. \tag{C7}$$

The windowed function is parametrized by a Gaussian envelope with a peak time which is the weighted mean of their peaks

$$t_0' = \frac{\sigma_w^2 t_w + \nu^2 t_0}{\sigma_w^2 + \nu^2}, \tag{C8}$$

and a spectral bandwidth which is the sum of their bandwidths

$$\sigma_0'^2 = \sigma_w^2 + \nu^2, \tag{C9}$$

since the windowed function is more compact in the time domain and consequently more broad in the spectral domain. In the general case of the six-parameter wavelet, σ_0' and t_0' are complex parameters; in the five-parameter case they are real as $\nu = \sigma_0$. The coefficients are obtained by expressing each of the power-series expansions in powers of $\sigma_0'(t-t_0')$ and determining their

Downloaded from https://academic.oup.com/gji/article/111/2/363/753853 by guest on 25 August 2022

product. These operations require the standard translation and product theorems for power series:

$$\sum_{k=0}^{\infty} p_k(x-x_0)^k = \sum_{m=0}^{\infty} q_m(x-x_1)^m; \qquad q_m = \sum_{k=0}^{\infty} \frac{(k+m)!}{m!\,k!}(x_1-x_0)^k p_{k+m}, \tag{C10}$$

$$\sum_{k=0}^{\infty} p_k x^k \sum_{m=0}^{\infty} q_m x^m = \sum_{k=0}^{\infty} r_k x^k; \qquad r_k = \sum_{m=0}^{k} p_m q_{k-m}. \tag{C11}$$

While (C6) is in the form of Gram–Charlier series, the operations of translation and multiplication have altered the coefficients such that $c_0 \neq 1$, and $c_1 \neq c_2 \neq 0$.

Filtering theorem

For a narrow-band Gaussian filter with centre frequency ω_i and bandwidth σ_i

$$F_{i+}(\omega) = f_0 \,\mathrm{Ga}\left(\frac{\omega-\omega_i}{\sigma_i}\right), \tag{C12}$$

where f_0 is the normalization constant $\sqrt{1+\sigma_0^2/\sigma_i^2}/\mathrm{Ga}\,[(\omega_i-\omega_0)/\sqrt{\sigma_i^2+\sigma_0^2}]$, the filtering theorem has the form

$$\begin{aligned} F_iC(t) &= \mathscr{R}e\left\{\frac{A}{\sqrt{2\pi}\,\nu} f_0\, e^{-i[\omega_0(t-t_1)]} \int_{-\infty}^{\infty} \mathrm{Ga}\left(\frac{\omega-\omega_i}{\sigma_i}\right) \mathrm{Ga}\left(\frac{\omega-\omega_0}{\nu}\right) \sum_{k=0}^{\infty} a_k \,\mathrm{He}_k\left(\frac{\omega-\omega_0}{\nu}\right) e^{-i(\omega-\omega_0)(t-t_0)}\, d\omega\right\} \\ &= \mathscr{R}e\left\{\frac{A'}{\sqrt{2\pi}\,\sigma_i'} e^{-i[\omega_i'(t-t_1)+(\omega_i'-\omega_0)(t_1-t_0)]} \int_{-\infty}^{\infty} \mathrm{Ga}\left(\frac{\omega-\omega_i'}{\sigma_i'}\right) \sum_{k=0}^{\infty} d_k \,\mathrm{He}_k\left(\frac{\omega-\omega_i'}{\sigma_i'}\right) e^{-i(\omega-\omega_i')(t-t_0)}\, d\omega\right\}, \end{aligned} \tag{C13}$$

with coefficients which are a double infinite sum

$$d_k = \left(\frac{\sigma_i'}{\nu}\right)^k \sum_{j=0}^{\infty} \left(\frac{-1}{2}\right)^j \left(1-\frac{\sigma_i'^2}{\nu^2}\right)^j \sum_{l=0}^{\infty} \frac{(2j+k+l)!}{j!\,k!\,l!} \left(\frac{\omega_i'-\omega_0}{\nu}\right)^l a_{2j+k+l}. \tag{C14}$$

The Gram–Charlier expansion in (C13) is parametrized by a new centre frequency ω_i' and half-width σ_i':

$$\omega_i' = \frac{\nu^2\omega_i + \sigma_i^2\omega_0}{\nu^2+\sigma_i^2}, \tag{C15}$$

$$\sigma_i'^2 = \frac{\nu^2\sigma_i^2}{\nu^2+\sigma_i^2}, \tag{C16}$$

which arise from the product of two Gaussians. The new scale factor A' is given by

$$A' = Af_0 \frac{\sigma_i'}{\nu} \mathrm{Ga}\left(\frac{\omega_i-\omega_0}{\sqrt{\sigma_i^2+\nu^2}}\right), \tag{C17}$$

and reduces to $A' = A$ in the case of a five-parameter wavelet.

The expression for the coefficients derives from applying the shift property of the Hermite polynomials (B6) to change the argument from $(\omega-\omega_0)$ to $(\omega-\omega_i')$ and then applying the scale property of Hermite polynomials (B7) to scale the bandwidth parameter from ν to σ_i'. These operations modify the coefficients such that $d_0 \neq 1$, and $d_1 \neq d_2 \neq 0$.

APPENDIX D: QUADRATIC DISPERSION

The analysis of generalized seismological data functionals presented in the text is based on the model of linear dispersion. While the linear term of the Taylor series for differential wavenumber is usually a good approximation, in some cases (such as fundamental-mode surface wave dispersion) it may be inadequate. Here we extend our analysis of cross-correlagrams to the case of quadratic dispersion. In order to minimize the algebraic complexity, we present expressions for the Gaussian-wavelet approximation rather than the complete Gram–Charlier expansions.

In the case of quadratic dispersion, the expression for the differential response operator $D(\omega)$ has the form

$$D(\omega) \cong \exp\{-\omega_0\delta\tau_q - (\omega-\omega_0)\delta\tau_a - \tfrac{1}{2}(\omega-\omega_0)^2\lambda + i[\omega_0\delta\tau_p + (\omega-\omega_0)\delta\tau_g + \tfrac{1}{2}(\omega-\omega_0)^2\mu]\}, \tag{D1}$$

where $\delta\tau_p$, $\delta\tau_g$, $\delta\tau_q$, and $\delta\tau_a$ are defined by (45)–(48) and

$$\mu \equiv x\,\mathscr{R}e\,\{\delta\ddot{k}(\omega_0)\}, \tag{D2}$$

$$\lambda \equiv x\,\mathscr{I}m\,\{\delta\ddot{k}(\omega_0)\}. \tag{D3}$$

μ and λ represent the real and imaginary parts of the curvature of the complex phase function. With this parametrization of the differential response operator, we obtain an expression for $C_{ff}(t)$ in the form of a six-parameter Gaussian wavelet (A4):

$$C_{ff}(t) = \mathscr{R}e\,\{Ae^{-i[\omega_c(t-t_1)]}\,\mathrm{Ga}\,[\nu(t-t_0)]\}, \tag{D4}$$

Downloaded from https://academic.oup.com/gji/article/111/2/363/753853 by guest on 25 August 2022

where $D(\omega)$ is expanded about $\bar{\omega}_f$ and $\nu^{-2} = \sigma_c^{-2} + i\gamma$. The six real variables of (D4) can be expressed in terms of the parameters of the differential response operator:

$$A = \frac{\sigma_c}{\bar{\sigma}_c} \frac{1}{\sqrt[4]{1+\sigma_c^4\gamma^2}} \exp\left[-\bar{\omega}_f(\delta\tau_q - \delta\tau_a) - \frac{1}{2}\left(\frac{\bar{\omega}_c^2}{\bar{\sigma}_c^2} - \frac{\omega_c^2}{\sigma_c^2} + \lambda\bar{\omega}_f^2\right)\right], \tag{D5}$$

$$\omega_c = \frac{\sigma_c^2}{\bar{\sigma}_c^2}\bar{\omega}_c - \sigma_c^2(\delta\tau_a - \lambda\bar{\omega}_f), \tag{D6}$$

$$\sigma_c^{-2} = \bar{\sigma}_c^{-2} + \lambda, \tag{D7}$$

$$t_1 = \frac{\bar{\omega}_f}{\omega_c}\delta\tau_p + \frac{(\omega_c - \bar{\omega}_f)}{\omega_c}\delta\tau_g + \frac{\mu}{2}[(\bar{\omega}_f - \omega_c)^2 - \sigma_c^2], \tag{D8}$$

$$t_0 = \delta\tau_g - \mu(\bar{\omega}_f - \bar{\omega}_c), \tag{D9}$$

$$\gamma = \mu. \tag{D10}$$

Following our earlier analysis of windowing and filtering the cross-correlation function, we derive an expression for F_iWC_{ff} in the case of the quadratic dispersion

$$F_iWC_{ff}(t) = \mathcal{R}e\,\{A'e^{-i[\omega_f(t-t_1')]}\,\mathrm{Ga}\,[\sigma_f(t-t_0')]\}, \tag{D11}$$

which depends on the complex-valued parameters A', ω_f, σ_f, t_0' and t_1'. The scale factor A' has the form

$$A' = \frac{\bar{\sigma}_{wc}\sigma_f}{\sigma_{wc}\bar{\sigma}_f}\mathrm{Ga}\left(\frac{\sigma_w\nu}{\sigma_{wc}}(t_w - t_0)\right)\frac{\mathrm{Ga}\left(\dfrac{\omega_i - \omega_c}{\sqrt{\sigma_i^2 + \sigma_{wc}^2}}\right)}{\mathrm{Ga}\left(\dfrac{\omega_i - \bar{\omega}_c}{\sqrt{\sigma_i^2 + \bar{\sigma}_{wc}^2}}\right)}A, \tag{D12}$$

with $\sigma_{wc}^2 = \sigma_w^2 + \sigma_c^2$. The frequency location and scale parameters are defined in an analogous fashion to the linear dispersion case (27 and 28)

$$\omega_f = \frac{\sigma_{wc}^2\omega_i + \sigma_i^2\omega_c}{\sigma_{wc}^2 + \sigma_i^2}, \tag{D13}$$

$$\sigma_f^2 = \frac{\sigma_{wc}^2\sigma_i^2}{\sigma_{wc}^2 + \sigma_i^2}. \tag{D14}$$

The time shift parameters are also modified by the operations of windowing and filtering

$$t_0' = \frac{\sigma_w^2 t_w + \sigma_c^2 t_0}{\sigma_w^2 + \sigma_c^2}, \tag{D15}$$

$$t_1' = t_1 - \frac{(\omega_f - \omega_c)}{\omega_f}(t_1 - t_0'). \tag{D16}$$

We may recover the expression for linear dispersion (55) from (D11) by setting μ and λ to zero.

APPENDIX E: SUM-OF-WAVELETS THEOREM

Given a complex spectrum $C(\omega)$ which may be represented as a sum over Gaussian wavelets

$$C_+(\omega) = \sum_{n=1}^{N} A_n \frac{\sqrt{2\pi}}{\nu_n} \exp i[\omega_n t_1^n + (\omega - \omega_n)t_0^n]\,\mathrm{Ga}\left(\frac{\omega - \omega_n}{\nu_n}\right), \tag{E1}$$

it can be approximated by a function which is itself a Gaussian wavelet in the canonical form

$$C_+(\omega) = A\frac{\sqrt{2\pi}}{\nu}\exp i[\bar{\omega}t_1 + (\omega - \bar{\omega})t_0]\,\mathrm{Ga}\left(\frac{\omega - \bar{\omega}}{\nu}\right)\left[1 + \sum_{k=3}^{\infty} a_k\,\mathrm{He}_k\left(\frac{\omega - \bar{\omega}}{\nu}\right)\right], \tag{E2}$$

with parameters which are defined by

$$1 = \sum_n B_n e^{i\varphi_n},$$

$$0 = \frac{1}{\nu}\sum_n B_n e^{i\varphi_n}[i\nu_n^2(t_0^n - t_0) + (\omega_n - \bar{\omega})], \tag{E3a–c}$$

$$0 = \frac{1}{2\nu^2}\sum_n B_n e^{i\varphi_n}\{(\nu_n^2 - \nu^2) + [\omega_n - \bar{\omega} + i\nu_n^2(t_0^n - t_0)]^2\},$$

Downloaded from https://academic.oup.com/gji/article/111/2/363/753853 by guest on 25 August 2022

where B_n and φ_n are complex quantities:

$$B_n = \frac{1}{\sqrt{2\pi}} \frac{A_n}{A} \mathrm{Ga}\,[\nu_n(t_0^n - t_0)], \tag{E4}$$

$$\varphi_n = (\omega_n t_1^n - \bar{\omega} t_1) + (\bar{\omega} - \omega_n) t_0. \tag{E5}$$

These three complex-valued equations were obtained from the first three coefficients of the Gram–Charlier expansion in (E2)

$$a_k = \frac{1}{\sqrt{2\pi}\, A k!} \sum_n \frac{A_n}{\nu_n} e^{i[\omega_n t_1^n - \bar{\omega} t_1 - (\omega_n - \bar{\omega}) t_0]} \int_{-\infty}^{\infty} e^{i[(\omega - \omega_n)(t_0^n - t_0)]} \mathrm{Ga}\left(\frac{\omega - \omega_n}{\nu_n}\right) \mathrm{He}_k\left(\frac{\omega - \bar{\omega}}{\nu}\right) d\omega, \tag{E6}$$

and their real and imaginary parts form a system of six non-linear, implicit equations corresponding to the six parameters of (E3) (A, $\bar{\omega}$, ν, t_0 and t_1). These parameters define the best-fitting Gaussian wavelet in the least-squares sense.

Downloaded from https://academic.oup.com/gji/article/111/2/363/753853 by guest on 25 August 2022